Hybrid nanomaterials for biomedical applications

Kathryn M. L. Taylor-Pashow,†[ab] Joseph Della Rocca,†[a] Rachel C. Huxford[a] and Wenbin Lin*[a]

Received 1st February 2010, Accepted 9th June 2010
DOI: 10.1039/c002073g

Hybrid nanomaterials, composed of both inorganic and organic components, have recently been examined as promising platforms for imaging and therapeutic applications. This unique class of nanomaterials can not only retain beneficial features of both the inorganic and organic components, but also provides the ability to systematically tune the properties of the hybrid material through the combination of functional components. This *feature article* will summarize recent advances in the design and synthesis of hybrid nanomaterials and their applications in biological and biomedical areas. The hybrid nanomaterials to be discussed fall into two main categories, silica based materials and nanoscale metal–organic frameworks. Their applications as imaging contrast agents and nanotherapeutics will be highlighted.

1. Introduction

In spite of rapid progress in our understanding of the fundamental biological processes underlying many diseases, we have yet to achieve comparable advances in the detection, diagnosis, and treatment of these diseases. Such a discrepancy mainly arises from the fact that most clinical imaging or therapeutic agents do not efficiently accumulate in the intended parenchymal sites due to their nonspecific distribution throughout the body. Conventional imaging and therapeutic agents thus require high doses and result in significant side effects.[1] Nanomaterials are novel systems with the potential to alleviate many of these issues, and have received an increasing amount of attention for imaging and therapeutic applications over the past 20 years.[2–5] Nanoparticulate imaging and therapeutic agents exhibit several advantages, including tunable size, high agent loading, tailorable surface properties, controllable or stimuli-responsive drug release kinetics, improved pharmacokinetics, and biocompatibility.[1,6,7] Nanoparticles can be specifically targeted to certain regions of the body (*i.e.* tumor regions) by conjugation with targeting ligands to enhance their accumulation in the intended parenchymal sites. They can also be engineered to contain multiple agents (*i.e.* imaging and therapeutic agents) for real-time monitoring of the drug uptake and/or therapeutic responses. Both of these features are difficult to achieve with conventional small molecule drugs. A large number of nanoparticle platforms for biomedical applications have received clinical approval or are in clinical trials.[2,4,8]

The nanoparticle platforms that have been extensively explored for biomedical applications are predominantly either purely inorganic or organic materials. The archetypical inorganic nanoparticles, quantum dots (QDs), are nanomaterials generally composed of elements from either groups II and VI or III and V.[9–13] They display unique optical properties, including sharp and symmetrical emission spectra, high quantum yields, broad absorption spectra, good chemical and photostability, and tunable size-dependent emission wavelengths.[11] As a result, they have been evaluated extensively for use as

[a] *Department of Chemistry, CB#3290, University of North Carolina, Chapel Hill, North Carolina 27599, USA*
[b] *Savannah River National Laboratory, Aiken, SC 29808, USA. E-mail: wlin@unc.edu*
† Contributed equally to this feature article.

Kathryn M. L. Taylor-Pashow

Kathryn M. L. Taylor-Pashow received a BS in chemistry from the College of William and Mary in 2004. She earned a PhD in Inorganic Chemistry under the direction of Prof. Wenbin Lin at the University of North Carolina in 2009. Her research focused on the development of hybrid materials for biomedical applications. After receiving her PhD, she joined the Savannah River National Laboratory as a Senior Scientist.

Joseph Della Rocca

Joseph Della Rocca obtained a BA in chemistry from Middlebury College in 2007 working under Professor Sunhee Choi. He is currently working towards a doctorate in chemistry under the supervision of Professor Wenbin Lin. His research focuses on the development of hybrid materials for biomedical applications.

optical imaging probes both *in vitro* and *in vivo*. Another class of inorganic nanoparticles that have been evaluated for biomedical imaging applications are metal oxides, such as superparamagnetic iron oxide nanoparticles (SPIO). Iron oxide nanoparticles have been used as contrast agents for magnetic resonance imaging (MRI), and one formulation of SPIO has received FDA approval for clinical use.[5] Gold nanoparticles with controllable morphologies have been extensively used for biological imaging applications as they can be engineered to exhibit strong absorption in the NIR region.[14–17] Gold nanoparticles have also been explored for photothermal therapy, where absorbed light by small gold nanoparticles (10–30 nm) is rapidly converted into thermal energy to lead to hyperthermia and cell death.

Purely organic nanoparticles have also found widespread use as imaging and therapeutic agents. Liposomes have been the most successful nanoparticle platform for biomedical applications, with several formulations clinically available.[8,18] These nanoparticles are composed of an aqueous core surrounded by a phospholipid bilayer and have been used to deliver a variety of therapeutic and imaging agents.[19–22] Surface modification of the lipid bilayer allows for long *in vivo* circulation times and targeting to specific regions.[7] There have been many reports on the use of polymeric hydrogel nanoparticles as delivery vehicles for imaging contrast agents and therapeutics.[23–33] Dendrimers and other hyper-branched organic polymers have also been extensively evaluated for their potential in imaging and drug delivery applicatons.[34–39]

Hybrid nanoparticles are composed of both inorganic and organic components that can not only retain the beneficial features of both inorganic and organic nanomaterials, but also possess unique advantages over the other two types. For example, the ability to combine a multitude of organic and inorganic components in a modular fashion allows for systematic tuning of the properties of the resultant hybrid nanomaterial. This feature article will cover two major classes of hybrid nanomaterials, namely silica-based nanomaterials and nanoscale metal–organic frameworks (NMOFs), that have been recently explored for imaging and therapeutic applications. While many nanoparticle platforms may be considered hybrid, we have chosen to restrict our discussion to silica-based nanomaterials and NMOFs that are closely examined in our laboratory for biomedical applications.

There are two major types of silica-based hybrid nanomaterials, solid silica particles and mesoporous silica nanoparticles (MSNs). Unlike solid silica particles, MSNs exhibit many unique properties such as high surface areas, tunable pore sizes, and large pore volumes. The imaging or therapeutic cargoes can be either directly incorporated in the silica matrix or grafted to the outer surface of the solid silica particles. MSNs can be functionalized with imaging or therapeutic agents in several ways, including loading of cargo into the pores, covalent grafting, and co-condensation of siloxy-derived cargoes.

NMOFs, also termed nanoscale coordination polymers (NCPs), are a new class of hybrid nanomaterials crafted from metal connecting points and organic bridging ligands. These materials can be tailored for biomedical applications by direct incorporation of functionalities into the framework or *via* post-synthesis modification of an existing framework structure.[40,41] Due to the presence of tunable pores and channels in many types of NMOF materials, it is also possible to encapsulate hydrophobic or charged agents into NMOFs through noncovalent interactions.[42–45] This feature article highlights recent advances in the design and synthesis of hybrid silica and NMOF nanoparticles and their applications in biomedical imaging and drug delivery.

2. Synthesis of hybrid nanomaterials

2.1 Silica nanoparticles

The synthesis and functionalization of silica nanoparticles has been extensively reviewed elsewhere;[46–48] we will only briefly mention the synthetic strategies here. Two major strategies are used to synthesize silica nanoparticles: the sol–gel synthesis and reverse microemulsion synthesis. The sol–gel synthesis of monodisperse solid silica particles ranging in size from 50 nm

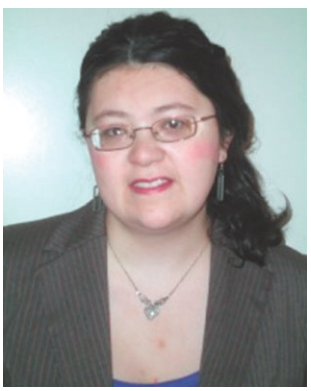

Rachel C. Huxford

Rachel C. Huxford received her BS in chemistry in 2007 from Tennessee Technological University. In 2008, she graduated from Tenn. Tech. with her MS in chemistry working under Prof. Edward Lisic. She is currently pursuing her doctorate degree in chemistry from the University of North Carolina at Chapel Hill under Prof. Wenbin Lin. Her current research involves the development of new hybrid materials for biomedical applications.

Wenbin Lin

Wenbin Lin obtained his BS degree from the University of Science and Technology of China (Hefei, China) in 1988. He received a PhD degree from the University of Illinois at Urbana-Champaign in 1994. Following a NSF postdoctoral fellowship at Northwestern University, he became an assistant professor of chemistry at Brandeis University in 1997. He joined the faculty of the University of North Carolina at Chapel Hill in 2001, receiving promotions to associate and full professor of chemistry in 2003 and 2007. His research focuses on developing hybrid materials for chemical, energy, and life sciences.

to 2 μm was first reported in 1968 by Stöber and co-workers.[49] This method involves the controlled hydrolysis and condensation of a silica precursor, such as tetraethyl orthosilicate (TEOS), in ethanol using ammonia as a catalyst (Fig. 1a). The size of the particles can be tuned by adjusting the reaction conditions. For example, adjusting the TEOS concentration from 0.05 M to 0.67 M while keeping the other reactant conditions constant affords silica particles from 20 to 880 nm in size.[50] These particles remain stable in solution due to electrostatic repulsion from the negatively charged silica particles. Another common method for the synthesis of monodisperse silica nanoparticles uses reverse phase, or water-in-oil, microemulsions (Fig. 1b).[51–53] Reverse phase microemulsions are highly tailorable systems that consist of nanometer-sized water droplets stabilized by a surfactant in a predominantly organic phase. The micelles in the microemulsion essentially act as ''nanoreactors'' that assist in controlling the kinetics of particle nucleation and growth. The size and number of micelles within the microemulsion can be tuned by varying the water to surfactant ratio (*W*). This method allows for careful control of particle size and polydispersity. The reverse microemulsion method is superior to the Stöber method for making monodisperse silica nanoparticles smaller than 100 nm.

The solid silica nanoparticles can be functionalized for biomedical applications using several methods. The simplest method is to entrap hydrophillic functional molecules within the silica matrix *via* noncovalent interactions. This method was widely used to incorporate luminescent dyes (such as the cationic fluorophore $Ru(bpy)_3)^{2+}$ within the anionic silica matrix.[55] However, the entrapped fluorophore can leach out of the nanoparticle under physiological conditions, potentially complicating the data interpretation. Alternatively, imaging or therapeutic agents can be covalently incorporated into silica nanoparticles by using trialkoxysilane-derived molecules that contain suitable imaging or therapeutic moieties. These molecules are incorporated within the silica matrix through silanol linkages during particle synthesis, leading to stable hybrid silica nanoparticles with uniform agents throughout the nanoparticle that are protected from the environment. The silica nanoparticles can also be post-synthetically modified by reacting with trialkoxysilane molecules. Post-synthesis grafting is particularly useful for modifying the particle surface with selected agents that are not stable during the silica particle synthesis. The synthetic versatility also allows the incorporation of imaging and therapeutic cargoes in multi-step sequences. After the desired organic functionality is attached to the silica nanoparticles, the nanoparticles can be further modified through the additional functional group using traditional conjugation chemistry. For example, an amine-modified particle can be reacted with various carboxylate-containing molecules to form a stable amide bond. The cargoes can also be conjugated to the nanoparticle surface by electrostatic interactions. Several types of other inorganic nanoparticles have also been embedded into the silica nanoparticle core to impart imaging functionalities.[56–58]

MSNs are typically synthesized using a surfactant-templated sol–gel method (Fig. 2).[59,60] They provide a unique platform for the development of hybrid nanoparticles due to their high surface areas and tunable pore structures. MCM-41 type materials, for example, possess a hexagonal array of one dimensional channels with diameters that can be tuned from 2–10 nm.[55,61] More recently, synthetic procedures have been developed for controlling the morphologies of MCM-41 materials,[62,63] leading to mesoporous silica nanospheres with diameters ranging from 60 to 1100 nm that have been utilized in a variety of applications, including catalysis,[64] drug delivery,[65,66] and imaging.[67–70]

MSNs can be covalently functionalized using two different approaches, either *via* co-condensation or by post-synthesis grafting. Victor Lin and coworkers have reported a co-condensation method for incorporating various organic functional groups into the pores of MSN.[60,71,72] The desired triethoxysilane is condensed into the walls of the MSNs during synthesis of the nanoparticle to lead to uniform incorporation

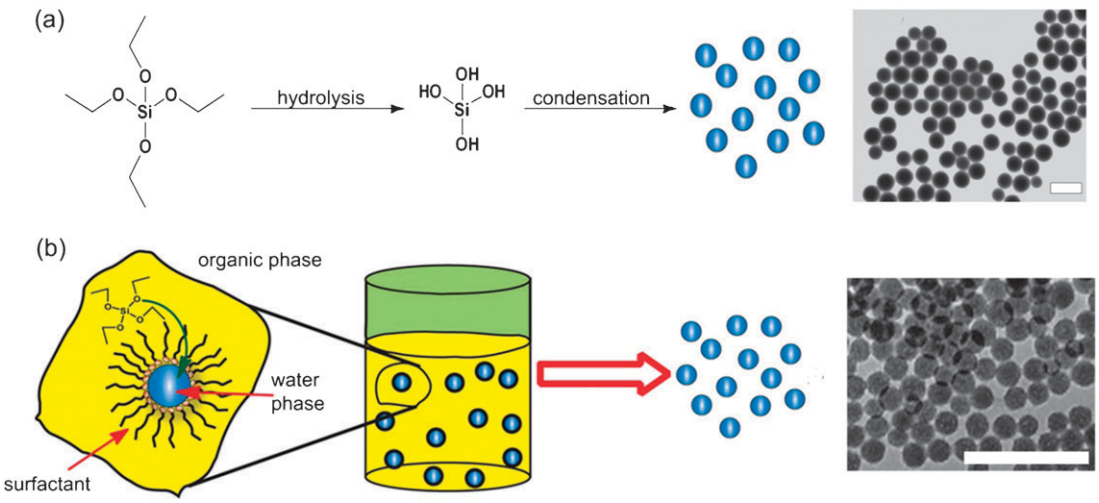

Fig. 1 Methods for synthesizing solid silica nanoparticles. (a) The Stöber method, in which the hydrolysis and condensation of TEOS is facilitated by base in ethanol/water: TEM micrograph shows 125 nm silica nanoparticles.[54] (b) The reverse phase microemulsion, in which TEOS is hydrolyzed at the micellar interface and enters the aqueous droplet to form a silica nanoparticle within the micelle. TEM micrograph shows 37 nm silica nanoparticles.[53] The scale bars indicate 200 nm. All TEM micrographs reproduced with permission.

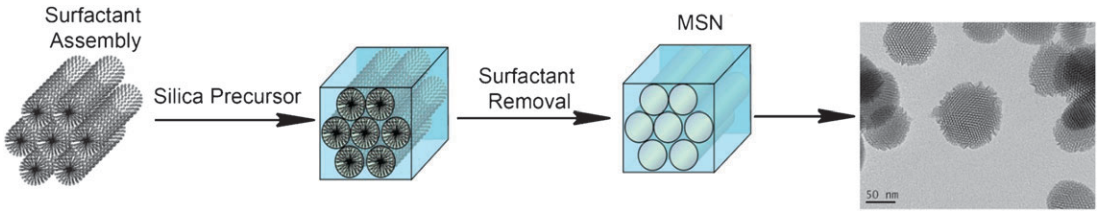

Fig. 2 Schematic showing synthesis of MCM-41 type MSN particles. The cationic surfactant molecules self-assemble into hexagonal arrays in aqueous conditions and the silica precursors then hydrolyze and condense along the exterior of the micelles to form a mesoporous material after extraction of the surfactant.

of the organic functionality throughout the particles. The degree of functionalization and the particle size can be modified by adjusting the reagent concentration, size, and the hydrophobicity or hydrophillicity of the co-condensing reagents. However, not all types of MSN nanoparticles can be made by this method, as the organically modified triethoxysilane can destabilize the surfactant templates during the synthesis, leading to large, rod-like particles ($\approx$1000 nm).[72] The organic functionality can also have a pronounced effect on the pore structure of the nanoparticle.

Alternatively, as-synthesized MSNs can be functionalized *via* post-synthesis modification, for example, by reacting MSN nanoparticles with a variety of trialkoxysilanes to effect condensation with the silanol group on the silica surface. This method allows the particle morphology and pore structure to remain intact, but has been found to lead to inhomogeneous surface coverage of the nanoparticle, as the particle exterior surface and pore entrances are kinetically more accessible. This feature can also be exploited to selectively modify the exterior surface of the nanoparticles before the extraction of the surfactant in the channels. The surfactant is then removed and the interiors of the pores can then be differentially functionalized. The organically modified MSN nanoparticles can be further modified with biomedically relevant molecules.

2.2 Nanoscale metal–organic frameworks (NMOFs)

Metal–organic frameworks (MOFs), or coordination polymers, are a new class of hybrid materials built from transition metal ions and polydentate bridging ligands. Bulk MOFs have shown promise in a number of applications, including nonlinear optics,[73] selective catalysis,[74] gas storage,[75,76] and chemical sensing.[77] By scaling the materials down to the nano-regime, these materials can be used for biomedical applications. In the silica-based nanomaterials described above, the silica matrix acts as a support for biomedically relevant moieties. In contrast, NMOF particles can have these moieties incorporated within the framework structure as either the metal connecting points or the bridging ligands. The various methods for synthesizing NMOF particles have recently been reviewed, so these methods will not be detailed here.[40] Briefly, NMOF nanoparticles are primarily synthesized by four methods: reverse microemulsion, surfactant-mediated hydrothermal synthesis, hydrothermal synthesis, and nanoprecipitation (Fig. 3). The first three methods generally lead to crystalline nanomaterials whereas the fourth method tends to afford amorphous nanomaterials.

Many of the NMOF materials tend to dissociate slowly in aqueous media, so they must be stabilized to increase their utility in biological applications. Our group was able to successfully encapsulate several NMOFs within a silica shell.[80–83] Briefly, the as-synthesized NMOFs were treated with polyvinylpyrollidone, then coated with a shell of amorphous silica using either TEOS as the silica source in basic ethanol or using sodium silicate in aqueous media. The silica shell thickness could be controlled by varying the reaction conditions. This coating significantly slows the release of the NMOF components to increase their circulation half-lives. For example, Tb-DSCP (DSCP = disuccinato-cisplatin) NCPs were coated with either 2 nm or 7 nm thick silica shells by varying the reaction time. Subsequent Pt release studies demonstrated that the uncoated nanoparticles have a half-life of approximately 1 hr, the 2 nm thick coating gave a half-life of 5.5 hours, and the 7 nm thick coatings had a half life of 9 hours.[81] Additionally, the surface of the silica-coated NMOFs could be further modified by using a variety of silyl-derived molecules. NMOF particles have also been coated with biocompatible polymers *via* coordination to the surface metal centers.[43,84] Horcajada and coworkers successfully conjugated several biocompatible polymers (poly(ethylene glycol), dextran, and chitosan) to a variety of iron-carboxylate NMOF particles. Boyes and coworkers have coated Gd-NMOFs previously described by the Lin group[78] with a copolymer of poly(N-isopropylacrylamide)-*co*-poly(N-acryloxysuccinimide)-*co*-(fluorescein O-methacrylate) by RAFT polymerization.[84] Additional imaging contrast agents or therapeutic moieties could be conjugated to the polymer through the succinimide group. Release studies showed that this polymer was able to impede, but not completely prevent, the release of Gd^{3+} ions from the NMOF.

3. Hybrid nanomaterials for imaging applications

3.1 Solid silica nanoparticles for imaging

There have been numerous reports on incorporating organic fluorophores into solid silica nanoparticles for optical imaging. In 2004, Tan and coworkers reported the synthesis of fluorescein isothiocyanate (FITC) doped silica nanoparticle probes in reverse microemulsions.[85] The resulting 70 nm nanoparticles were conjugated with the TAT peptide, a cellular penetrating peptide, and used to label human lung cancer cells *in vitro*. The *in vivo* utility of these nanoparticles was demonstrated by selectively labeling rat brain blood vessels *via* intra-arterial

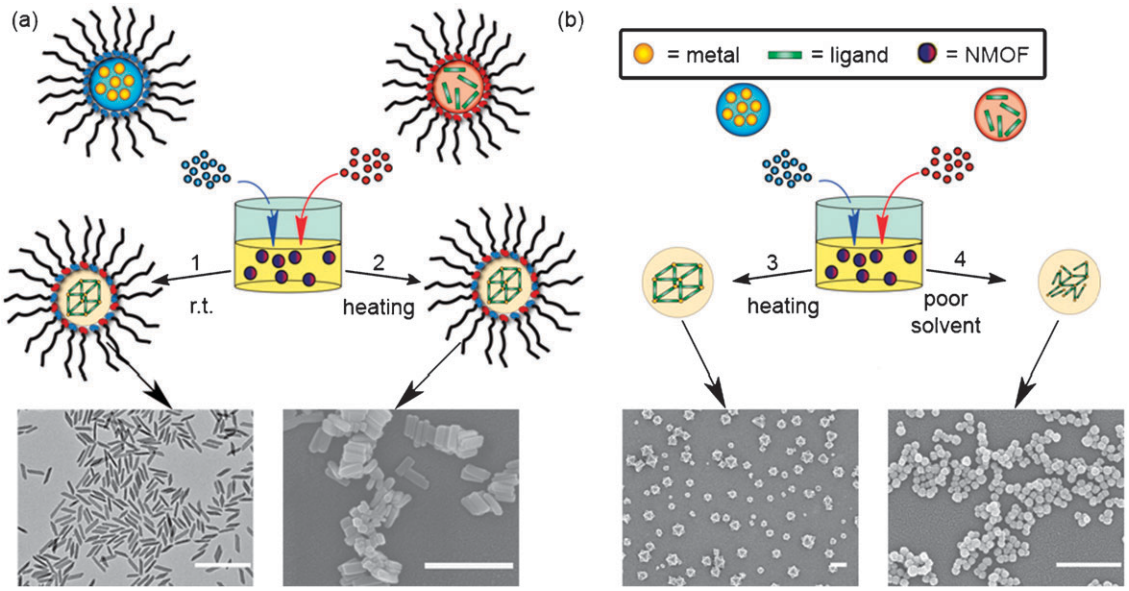

Fig. 3 Schematic showing various methods for making NMOF materials. (a) Water-in-oil microemulsion methods: the microemulsions are stirred at room temperature (1) or heated (2). (b) Non-surfactant mediated methods: heating a solution of the metal and the ligand in a coordinating solvent (3) or adding a poor solvent to a solution of the metal and the ligand at room temperature (4). EM micrographs show NMOFs of Gd-BDC (BDC is 1,4-benzenedicarboxylate),[78] Gd-BHC (BHC is benzenehexacarboxylate),[79] MIL-101 ($Fe_3(\mu_3\text{-}O)Cl(H_2O)_2(BDC)_3$),[80] and Tb-DSCP (DSCP is disuccinato-cisplatin)[81] from left to right. Scale bars indicate 500 nm. All SEM micrographs were reproduced with permission.

delivery. After the procedure was completed, the brain was imaged using fluorescence microscopy, and nanoparticle fluorescence was observed in brain vessels. These results showed that the TAT-conjugated nanoparticles could selectively cross the blood brain barrier and serve as a potential way to deliver diagnostic or therapeutic agents to the brain.

In 2005, Wiesner and coworkers reported the synthesis and characterization of core–shell fluorescent silica nanoparticles, referred to as CU dots.[86] These 20–30 nm particles, synthesized using a modified Stöber method, consisted of a fluorophore-rich core protected with a siliceous shell. The CU dots are approximately 20 times brighter than the constituent dye. Wiesner, Nikitin, and coworkers later reported a similar synthesis of core–shell fluorescent silica nanoparticles synthesized using the Stöber method, known as C-dots.[87] The *in vivo* efficacy of these particles as optical imaging contrast agents was demonstrated using multiphoton microscopy. No apparent toxicity in the mice was observed. Enhanced intracellular delivery of C-dot nanoparticles was achieved by modifying the surface properties.[88] HeLa cells internalized twice the amount of C-dot particles that were electrostatically coated with a cationic polymer, polyethyleneimine (PEI), relative to the unfunctionalized C-dots. Neither the C-dots nor the PEI coated C-dots showed appreciable toxicity to COS-7 cells over all concentrations tested.

In 2007, Ishimura and coworkers also reported the synthesis of dye-doped silica nanoparticles with organic fluorophores incorporated throughout the nanoparticle.[89] These nanoparticles ranged from 300 nm to 450 nm in diameter. The *in vivo* labeling of these nanoparticles was evaluated by intraperitoneally injecting nanoparticles into mice. No apparent toxicity was observed after injection. After 1 week, the peritoneal cells were harvested and then examined by confocal and electron microscopy. Confocal microscopy clearly showed fluorescently labeled cells with nanoparticles distributed throughout the cellular cytoplasm and on the membrane surface. Further electron microscopy studies revealed that the labeled cells were macrophages, while other cells showed no fluorescent labeling.

Wiesner, Bradbury, and coworkers recently reported the synthesis of smaller C-dots with hydrodynamic diameters of 3.3 and 6.0 nm.[90] These particles contained the near-IR dye molecule Cy5 and had improved photophysical properties. *In vivo* studies in mice showed that these small particles could be cleared through the kidneys and the liver. Surface modification with poly(ethylene glycol) (PEG) showed increased kidney filtration and decreased liver uptake compared to the uncoated particles (Fig. 4). Biodistribution studies of the 3.3 nm and 6.0 nm particles displayed minimal particle retention in the major organs, with most of the fluorescence localized within the bloodstream. The particles were completely cleared after 48 hours. The larger particles (6.0 nm) exhibited a longer tissue half-life and greater organ retention.

Prasad and coworkers functionalized dye incorporated silica nanoparticles with a variety of active groups including hydroxyl, thiol, amine, and carboxyl.[91] The surface characteristics of nanoparticles play an important role in the uptake of particles by certain types of cells. For example, amino-terminated particles were taken up more efficiently by pancreatic cancer cells than carboxyl-terminated particles. The carboxyl groups present on the carboxyl-terminated particles were used to conjugate various bioactive molecules, such as transferrin and the monoclonal antibodies anti-claudin 4 and anti-mesothelin, allowing for targeted delivery to pancreatic cancer cells. The increased uptake of these targeted particles was demonstrated *in vitro*. A similar experiment was demonstrated by He and coworkers,[92] who successfully functionalized the

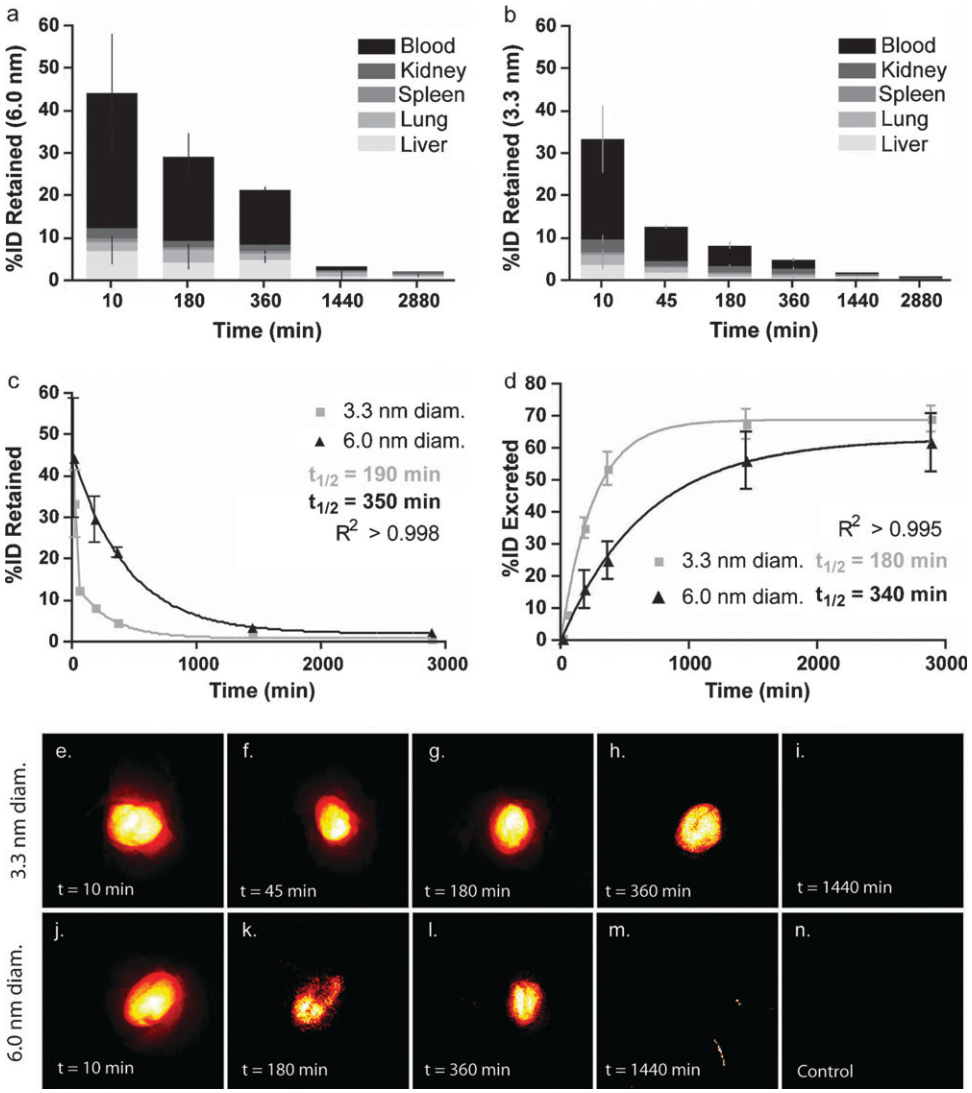

Fig. 4 Biodistribution analysis of the C-dot nanoparticles in mice (top) and fluorescent pseudo-color imaging of mice bladders *ex vivo* (bottom). Reproduced with permission from ref. 90.

surface of silica nanoparticles containing Nile Red with amine groups and conjugated the targeting moieties apo-transferrin and folic acid. Both of these targeting moieties resulted in increased uptake of the particles by HeLa cells *in vitro*.

Wang and Tan have reported the synthesis and characterization of multicolor FRET silica nanoparticles.[93] A modified Stöber method was used to synthesize the particles, and three different dyes were incorporated into each nanoparticle. By adjusting the ratio of the tandem dyes, the fluorescence resonance energy transfer (FRET)-mediated emission signatures could be tuned. The resulting nanoparticles exhibit multiple colors under a single wavelength excitation (Fig. 5). The particles were post-modified to contain different surface functional groups, and then conjugated with an aptamer and biotin. The NP-biotin complexes were conjugated onto the surface of strepavidin-microspheres for multicolor barcoding applications. Preliminary *in vitro* assays using aptamer-conjugated nanoparticles displayed efficient labeling of cancer cells with little photobleaching as observed by confocal microscopy.

Luminescent metal complexes such as tris(2,2′-bipyridyl)-dichlororuthenium(II) ($Ru(bpy)_3^{2+}$) have also been incorporated into silica nanoparticles for optical imaging.[55,94] The large Stokes shift of the $[Ru(bpy)_3]Cl_2$ fluorophore significantly reduces the background signal from biological systems. $[Ru(bpy)_3]Cl_2$ is also much more photostable than organic fluorophores such as fluorescein. The fluorescence spectra, particle size, and size distribution of Ru(bpy) dye-doped silica nanoparticles were examined as a function of reactant concentrations (TEOS and ammonium hydroxide), nature of surfactant molecules, and molar ratios of water to surfactant (W) and co-surfactant to surfactant, in order to optimize synthetic conditions.[55] Tan and coworkers conjugated an antibody onto the surface of the as-synthesized nanoparticles in order to selectively label leukemia cells for optical microscopy.[94] *In vivo* behaviors of these nanoparticles were recently reported.[95] Pegylated $Ru(bpy)_3^{2+}$ dye-doped silica nanoparticles exhibited long blood circulation times and minimal RES organ uptake, whereas non-pegylated particles were cleared from the blood stream within 3 hours post injection and showed

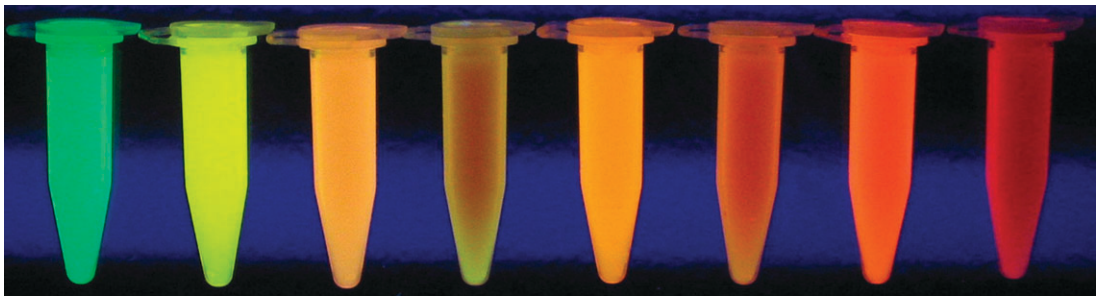

Fig. 5 FRET Silica nanoparticle samples with different doping dye combinations under 300 nm UV illumination. Dye doping ratio (in order) (FITC : R6G : ROX): 1 : 0 : 0, 0 : 1 : 0, 1 : 0 : 1, 4 : 1.5 : 3, 0.5 : 0.5 : 0.5, 2 : 2 : 2, 0 : 1 : 1, 0.5 : 0.5 : 4. Reproduced with permission from ref. 93.

significant accumulation within typical RES organs (Fig. 6). *Ex vivo* analysis of organs confirmed the optical imaging results.

Silica nanoparticles have also been used as a platform for developing improved contrast for magnetic resonance imaging (MRI). The use of a nanoparticle platform provides several advantages over small molecule contrast agents. The increased size results in reduced tumbling rates, which increases the relaxivity. The decreased tumbling rate of nanoparticles is closer to the Larmor frequency of the protons, increasing the efficiency of relaxation. Each nanoparticle can deliver a high payload of paramagnetic metals, making the system amenable to targeting. Several groups have also demonstrated the combination of optical and MR contrast enhancing ability

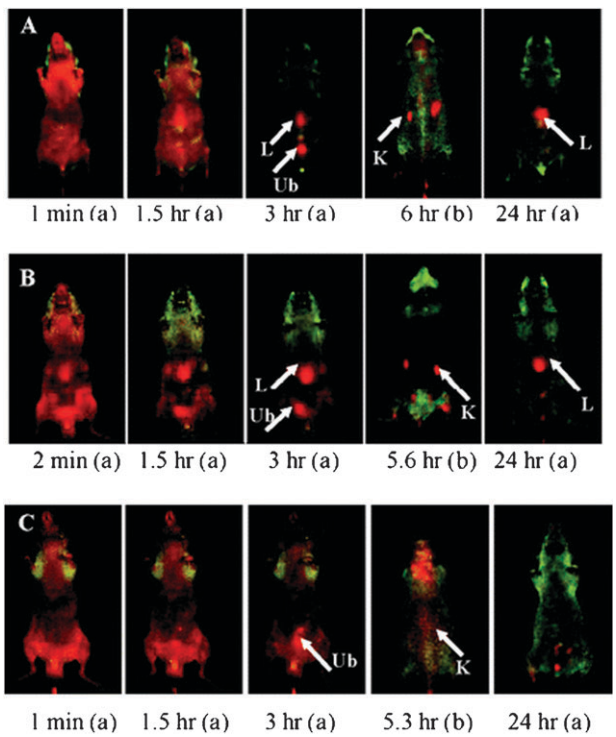

Fig. 6 *In vivo* imaging of the biodistribution of different iv injected surface-modified SiNPs (A–C) at different time points post-injection ((a) abdomen imaging; (b) back imaging). (A) OH-SiNPs; (B) COOH-SiNPs; (C) PEG-SiNPs. Arrows mark the location of the kidney (K), liver (L), and urinary bladder (Ub). Reproduced with permission from ref. 95.

in a single platform, allowing for two modes of imaging within a single particle system.[53,57,58,96–99]

Our group prepared 37 nm hybrid silica nanoparticles containing an embedded $[Ru(bpy)_3]Cl_2$ luminophore and a shell of Gd chelates for use as a dual optical and MR contrast agent.[53] The Gd chelates were immobilized onto the surface of the silica nanoparticles in either a monolayer or multilayer fashion. The surface-immobilized Gd chelates effectively relax water protons. The resulting nanoparticle has relaxivities five orders of magnitude higher than the constituent Gd chelate due to the greatly increased Gd payload as well as the much enhanced per Gd relaxivity as a result of the reduced tumbling rates. Notably, the particles with multilayers of Gd chelates had reduced relaxivities compared to those with the monolayer coating, likely due to reduced water accessibility of the Gd chelates. Murine monocyte cells were successfully labeled with the hybrid silica nanoparticles and T_1- and T_2-weighted signal enhancement of the cell pellet was observed in a 3 T MR scanner (Fig. 7).

The efficacy of the hybrid silica nanoparticles as a dual optical and MR contrast agent was also demonstrated in a collagen-induced arthritis (CIA) mouse model at 9.4 T.[96] Mice were injected with saline, 125 mg/kg, or 250 mg/kg of hybrid silica nanoparticles in two doses separated by 6 hours. Luminescence intensity of the paws was measured with a clinical scanner the following day. All control mice displayed minimal luminescence compared to those which received the nanoparticle dose (Fig. 8). The level of luminescence corresponded with the dose received, the clinical disease index, and the level of paw swelling. MRI imaging showed a 33–35% reduction in the T_2 signal of mice treated with the nanoparticle agent; however, no T_1 enhancement was observed (Fig. 9). Tissue histopathological analysis demonstrated that the particles were located within the synovial tissue where disease was present and nanoparticle luminescence nicely co-registered with the fluorescence of the antibody that labeled monocyte cells.

We have developed a polyelectrolyte layer-by-layer (LbL) self-assembly approach to circumvent the reduced relaxivities found in the solid silica particles with multilayer coatings.[97] Positively charged Gd chelate oligomers were deposited onto negatively charged silica nanoparticles possessing a Gd-DTTA (DTTA = diethylenetriamine tetraacetate) monolayer *via* electrostatic interactions. The resulting positively charged particle was further treated with negatively charged

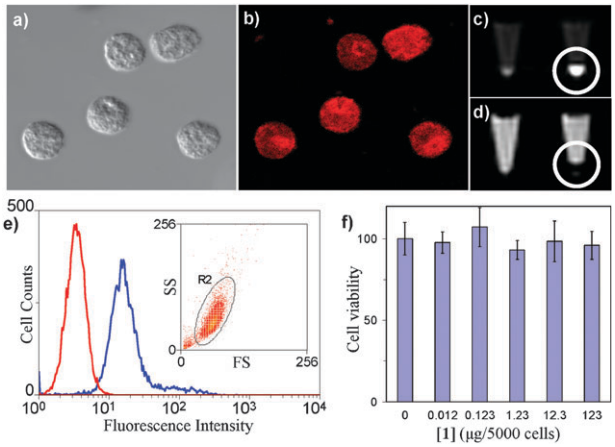

Fig. 7 Microscopic images of labeled monocyte cells: (a) optical; (b) laser scanning confocal fluorescence. (c, d) MR images of unlabeled (left) and labeled (right) monocyte cells: (c) T_1-weighted and (d) T_2-weighted. (e) Flow cytometric results for the unlabeled (red) and labeled (blue) monocyte cells indicating greater than 98% labeling efficiency (the inset shows the purity of the labeled cells; SS = side scatter, FS = forward scatter). (f) MTS cell viability assay of the monocyte cells incubated with different amounts of nanoparticle. Reproduced with permission from ref. 53.

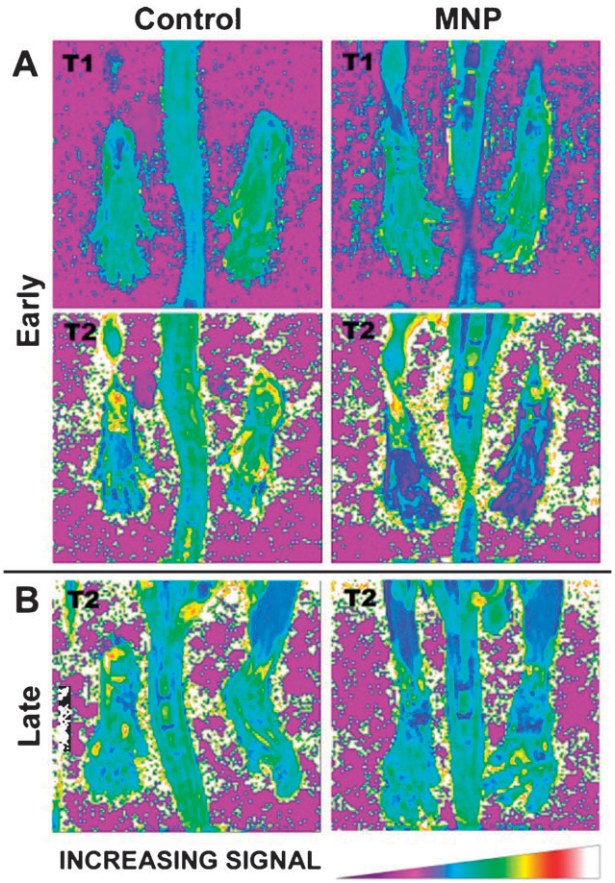

Fig. 9 (A) Representative T_1 and T_2 relaxation map of the hindlimbs of a mouse with early stage CIA before and after MNP administration. (B) T_2 relaxation maps of hindlimbs from a mouse with later stage CIA before and after receiving contrast agent. Reproduced with permission from ref. 96.

polystyrenesulfonate (PSS) to provide a net negative charged layer. These steps were repeated to form the LbL multilayer architecture. TEM and fluorescence studies indicated the consecutive deposition of polymeric electrolytes onto the particle, whereas MR phantom studies demonstrated that nanoparticles with more layers of the Gd-DOTA (DOTA = Cyclen-1,4,7,10- tetraacetate) polymers had the expected higher relaxivities on a per particle basis. The relaxivities on a per Gd basis remained constant, regardless of the number of layers deposited. The LbL self-assembly, thus, increases the Gd payload without deleteriously affecting the MR relaxivity on a per Gd basis, presumably as a result of the flexible and disordered nature of the polyelectrolyte LbL assembly which allows the surrounding water molecules access to the Gd(III)

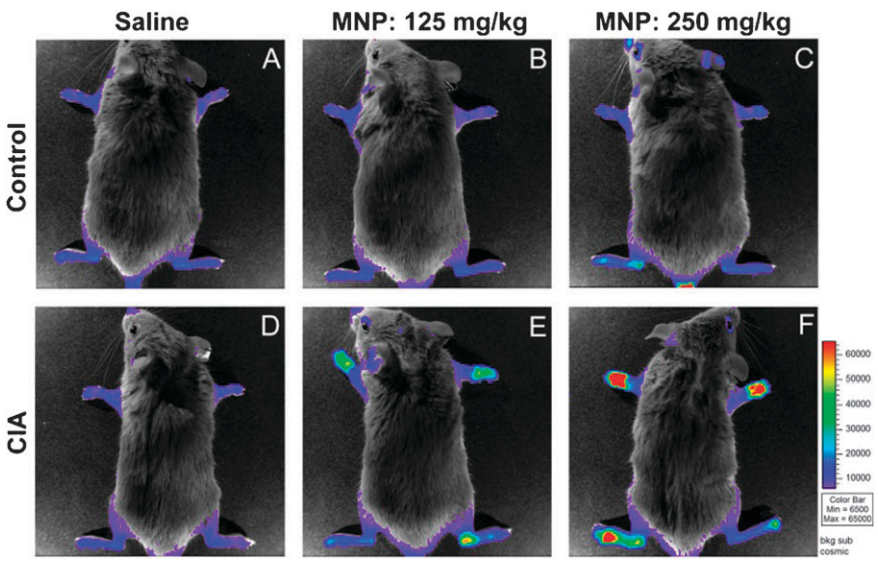

Fig. 8 (Top) Control animals that did not have arthritis intravenously injected with two separate doses of (A) saline, (B) 125 mg MNP/kg, or (C) 250 mg MNP/kg 12 hours before optical imaging. (Bottom) CIA animals with arthritis intravenously injected with (D) saline, (E) 125 mg MNP/kg, or (F) 250 mg/kg. Reproduced with permission from ref. 96.

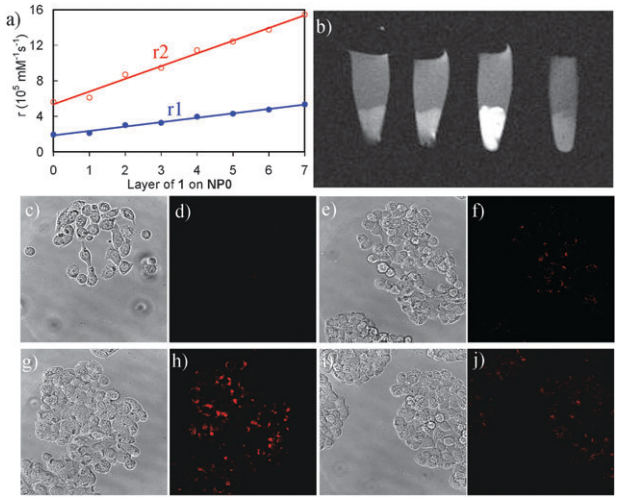

Fig. 10 (a) Dependence of per particle r_1 and r_2 values on the number of deposited Gd–DOTA oligomer layers. (b) T_1-weighted MR images of HT-29 cells that have been incubated with various nanoparticles. From left to right: control cells without any nanoparticle, cells with LbL particles, cells with LbL particles that have been noncovalently functionalized with K_7RGD, and cells with LbL particles that have been noncovalently functionalized with K_7GRD. (c–j) Phase contrast optical (c, e, g, and i) and LSCFM microscopic images (d, f, h, and j) of HT-29 cells that have been incubated with various nanoparticles: control cells without any nanoparticle (c and d), cells with LbL particles (e and f), cells with LbL particles that have been noncovalently functionalized with K_7RGD (g and h), and cells with LbL particles that have been noncovalently functionalized with K_7GRD (i and j). Reproduced with permission from ref. 97.

centers. A peptide sequence containing arginine-glycine-aspartate (RGD) and seven consecutive lysine (K) residues (K7RGD) was adsorbed onto the particles terminated with a negatively charged PSS layer *via* electrostatic interactions. The RGD peptide is known to bind strongly to the integrin cell surface receptors that are upregulated in angiogenic cancer cells. The RGD-terminated nanoparticles allowed target-specific optical and MR imaging of HT-29 human colon cancer cells (Fig. 10).

Gd chelates have also been incorporated into quantum dots (QDs)@silica or Au@silica core–shell nanostructures.[58,100,101] The QDs or Au nanoparticles in the cores provided the optical contrast whereas the Gd chelates gave the T_1-weighted MRI enhancements. Blood circulation of these nanoparticles was also studied *in vivo*.

3.2 Mesoporous silica nanoparticles for imaging

Nanoparticulate MR contrast agents have also been constructed based on MSNs in order to take advantage of their high internal surface areas.[68,70,102] In 2008, our group reported the synthesis of an efficient MR contrast agent based on MSN particles with MCM-41 type pore structure.[70] The extremely high surface area of MSN allows for a high payload of Gd chelates with enhanced water accessibility, which is key to high r_1 relaxivity. MSNs were first prepared by a surfactant-templated, base-catalyzed condensation of TEOS. Subsequently, a monolayer of Gd-chelates was grafted by refluxing in toluene. The resulting MSNs exhibited exceptionally high relaxivities both on a per Gd and a per particle basis. On a

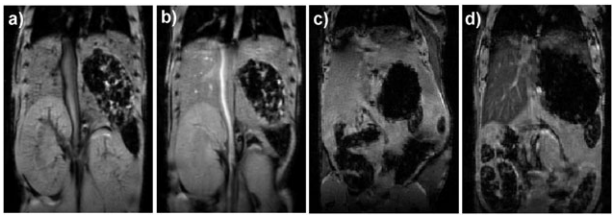

Fig. 11 (a) Pre-contrast and (b) post-contrast (2.1 μmol/kg dose) T_1-weighted mouse MR images showing aorta signal enhancement. (c) Pre-contrast and (d) post-contrast (31 μmol/kg dose) mouse MR images showing liver signal loss due to T_2-weighted enhancement. Reproduced with permission from ref. 70.

per mM Gd basis, the MSN-Gd had an r_1 of 28.8 mM^{-1} s^{-1} and an r_2 of 65.5 mM^{-1} s^{-1} at 3 T. Since each particle contains approximately 36 900 Gd ions, the r_1 and r_2 values on a per mM of particle basis were 1.06×10^6 mM^{-1} s^{-1} and 2.42×10^6 mM^{-1} s^{-1}, respectively. The contrast enhancing ability of these particles was also demonstrated *in vivo*. Significant T_1-weighted signal enhancement was seen in the aorta of a mouse 15 minutes after intravenous injection of a dose of MSN-Gd corresponding to 2.1 μmol Gd per kg of body weight (Fig. 11a,b). This dose is approximately 100-fold lower than what is currently used for commercially available Gd-chelate contrast agents. At a higher dose of 31 μmol/kg, T_2-weighted signal enhancement was observed in the liver 1 hour after administration (Fig. 11c,d).

Huang and coworkers reported the synthesis of MR-enhancing MSNs by a post-synthesis Gd loading strategy.[102] 120 nm MSNs were synthesized by co-condensing FITC-APTMS, silyl-derived DTPA, and TEOS using cetyl trimethylammonium bromide (CTAB) as a structure directing agent, and then loaded with Gd^{3+} ions. Relaxivity measurements revealed an r_1 value of 23 mM^{-1} s^{-1} and an r_2 value of 34 mM^{-1} s^{-1} at 1.5 T. MR studies also demonstrated cell labeling at high doses. Cellular uptake of the Gd-dye@MSN nanoparticles was investigated by flow cytometry and showed that the uptake was time and dose dependent. These nanoparticles were also used to label stem cells *in vitro*. Labeled stem cells were injected into nude mice and then visualized by MRI for up to 14 days.

Lindén and coworkers have developed a functionalized MSN nanoparticle system for delivery of imaging agents to cancer cells.[103,104] First, amine-functionalized MSNs were prepared and then hyperbranched poly(ethylene imine) polymers were grown on the surface *via* surface polymerization. The nanoparticles were then labeled with silyl-derived FITC and targeted using folic acid. Preliminary *in vitro* HeLa cell assays demonstrated that the targeted nanoparticles had a 5-fold higher internalization compared to the non-targeted control and could be used to specifically target folate-receptor expressing cells specifically in co-culture conditions.

3.3 Nanoscale metal–organic frameworks for imaging

NMOFs have shown promise for applications in both magnetic resonance imaging (MRI) and computed tomography (CT).[43,78,79,83,84,105] Gd-based NMOFs have been shown to enhance image contrast in MRI. For example, $Gd_2(BDC)_3(H_2O)_4$

(BDC = 1,4-benzenedicarboxylate) nanorods synthesized by our group (approximately 100 nm in length by 40 nm in diameter) gave an r_1 of 35.8 mM^{-1} s^{-1} in an aqueous xanthan gum suspension (Fig. 12a).[78] This value is almost an order of magnitude higher than that obtained with the commercially available T_1-weighted contrast agent Omniscan. More importantly, the relaxivities on a per particle basis were extraordinarily high, owing to the presence of a large number of Gd^{3+} centers in each particle. These NMOFs can also be rendered luminescent by doping with emissive lanthanide ions such as Eu^{3+} or Tb^{3+} to afford luminescent nanoparticles (Fig. 12b). Organic linkers such as BDC act as antenna to absorb light and transfer its excitation energy to the lanthanide ions. Similar relaxivities and luminescent properties were obtained for $Gd_2(BHC)(H_2O)_6$ NMOFs synthesized using a surfactant-mediated synthesis method.[79] Unfortunately, Gd NMOFs leached μM concentrations of Gd^{3+} ions in water, which precluded their *in vivo* applications as MRI contrast agents, due to the toxicity of free Gd^{3+} ions. Attempts were made to stabilize the NMOFs by coating them with a silica shell.[82] The release of Gd^{3+} ions from the NMOF-silica core–shell nanostructures was significantly retarded but not entirely eliminated. In addition, it was possible to surface functionalize the nanoparticles using a variety of silyl-derived ligands.

To address the toxicity issue with leached Gd^{3+} ions from Gd NMOFs, the Lin group has synthesized Mn-based NMOFs and evaluated their use as MR contrast agents.[83] Nanorods of $Mn(BDC)(H_2O)_2$ were found to have an r_1 of 5.5 and an r_2 of 80.0 mM^{-1} s^{-1} on a per Mn basis at 3 T, whereas nanorods of $Mn_2(BTC)_3(H_2O)_6$ exhibited an r_1 of 7.8 and an r_2 of 70.8 mM^{-1} s^{-1} on a per Mn basis. The Mn-NMOF-silica nanostructures were also functionalized with rhodamine B and a targeting peptide, cyclic-(RGDfK), for cancer imaging. Confocal fluorescence microscopy and MRI studies indicated that the cyclic-(RGDfK)-targeted particles with a $Mn_3(BTC)_2(H_2O)_6$ NMOF core and a silica shell exhibited enhanced uptake by HT–29 angiogenic human colon adenocarcinoma cells, as compared to non-targeted particles (Fig. 13).

Our group has recently reported the synthesis and characterization of NMOF contrast agents for CT imaging.[105] NMOF nanoparticles were constructed from Cu^{2+} or Zn^{2+} and 2,3,5,6-tetraiodo-1,4-benzenedicarboxylic acid (I_4-BDC). Phantom CT images for both the Cu^{2+} and Zn^{2+} nanoparticles were obtained at various iodine concentrations and compared against a clinically used contrast agent, Iodixanol, at the same iodine concentrations. Both of these particles contain 63 wt% iodine, compared to 49 wt% for Iodixanol. Both nanoparticles were shown to have comparable efficiency to Iodixanol by comparison of the slopes obtained when Hounsfield Unit (HU) values were plotted against iodine concentrations. The slopes of HU *vs.* [I] for $[Cu(I_4\text{-BDC})(H_2O)_2]\cdot 2H_2O$, $[Zn(I_4\text{-BDC})(EtOH)_2]\cdot 2EtOH$, and Iodixanol were 4653 ± 520, 4513 ± 408, and 3840 ± 560, respectively (Fig. 14). These particles are attractive as CT contrast agents not only due to their efficiency to attenuate X-rays, but also for their biodegradable nature. Dialysis of the Cu^{2+} phase particles against phosphate buffered saline (PBS) at 37 °C showed that these particles had completely degraded within 46 h, with a half-life of 1.5 h.

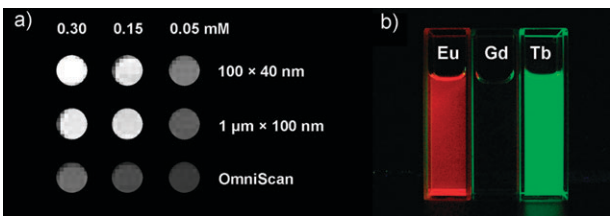

Fig. 12 (a) T_1-weighted MR images of suspensions of $Gd_2(BDC)_3(H_2O)_4$ nanorods in water containing 0.1% xanthan gum. (b) Luminescence images of ethanolic suspensions of $Gd_2(BDC)_3(H_2O)_4$ nanorods doped with 5 mol% Eu^{3+} or Tb^{3+}. Reproduced with permission from ref. 78.

4. Therapeutic applications of hybrid nanomaterials

4.1 Silica-based materials for therapy

Hybrid silica nanoparticles have been used in drug delivery and therapy applications. Prasad and coworkers described the use of an organically modified silica nanoparticle for photodynamic therapy (PDT).[106] PDT is a light-activated treatment for cancer and other diseases, and works by utilizing light sensitive drugs (*i.e.* photosensitizers) that can be preferentially localized in malignant tissues. Its therapeutic effect is initiated by photoexcitation of the localized photosensitizer to generate cytotoxic species such as singlet oxygen ($^1O_2$). This leads

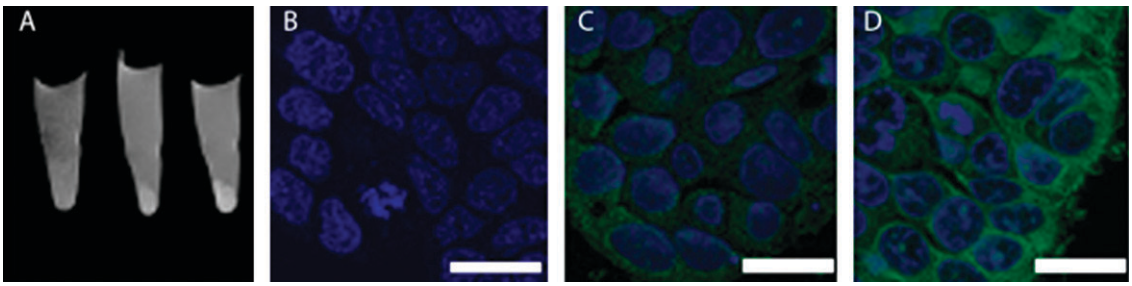

Fig. 13 (A) MR images of HT-29 cells incubated with Mn-based NMOFs, increasing concentrations from left to right. (B–D) Confocal images of HT-29 cells incubated with no particle (B), non-targeted Mn-NMOFs (C), and cRGDfK-targeted Mn-NMOFs (D). The cell nuclei were stained with DRAQ5 (blue) and particles were detected with rhodamine B (green). Scale bars represent 20 μm. Reproduced with permission from ref. 83.

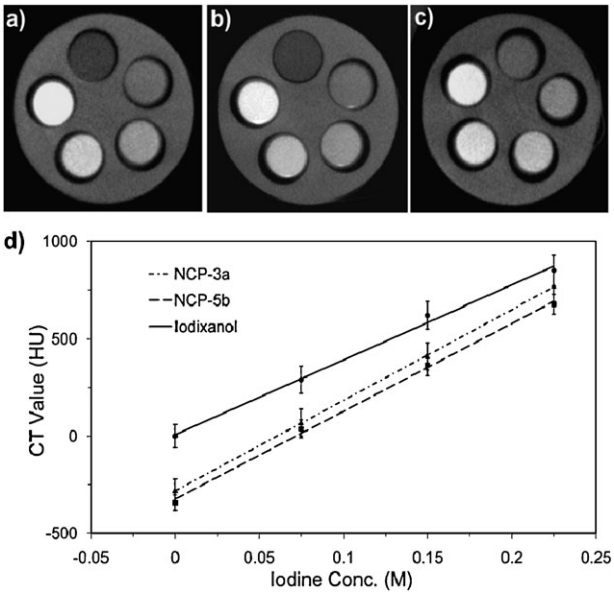

Fig. 14 CT phantom images of (a) $[Cu(I_4\text{-BDC})(H_2O)_2]\cdot 2H_2O$ nanoplates, (b) $[Zn(I_4\text{-BDC})(EtOH)_2]\cdot 2EtOH$ nanoparticles dispersed in ethanol, and (c) Iodixanol in aqueous solution. From the top, clockwise, the slots have [I] = 0, 0.075, 0.150, 0.225, and 0.300 M. (d) X-ray attenuation as a function of [I] for $[Cu(I_4\text{-BDC})(H_2O)_2]\cdot 2H_2O$ nanoplates at 40 kVp, $[Zn(I_4\text{-BDC})(EtOH)_2]\cdot 2EtOH$ nanoparticles at 50 kVp, and Iodixanol at 40 kVp. Reproduced with permission from ref. 105.

to selective and irreversible destruction of diseased tissues, without damaging adjacent healthy ones. The main drawback to this therapy is that currently approved PDT photosensitizers absorb in the visible spectral region below 700 nm, where light penetration into the skin is only a few millimeters. This problem can be overcome by combining a two-photon absorbing (TPA) dye with the photosensitizer. Here, the photosensitizer is indirectly excited through fluorescence resonance energy transfer (FRET). In this work, a known photosensitizer and a two-photon energy donor were co-encapsulated in a $\sim$30 nm silica nanoparticle (Fig. 15). Upon two-photon irradiation, the photosensitizer is excited as a result of intraparticle FRET from the two-photon absorbing dye, resulting in the generation of singlet oxygen. The uptake of these particles was demonstrated through fluorescence imaging of HeLa cells. Upon two-photon irradiation, HeLa cells that had been incubated with the nanoparticles exhibited drastic morphology changes associated with cell necrosis, apparently induced by the reactive oxygen species generated by the photosensitizer.

A similar strategy was used by Hai and coworkers to prepare 105 nm silica particles with entrapped methylene blue (MB) dyes for near-IR (NIR) imaging and photodynamic therapy.[107] Methylene blue is an effective photosensitizer due to its high quantum yield of $^1O_2$ generation, low dark toxicity, and NIR therapeutic window. PDT was demonstrated *in vitro* against HeLa cells. Significant cell death was only observed in cells treated with the MB nanoparticles and laser irradiation, with little toxicity observed when the cells were treated with either the nanoparticles or the laser alone. Both fluorescence imaging and PDT was observed *in vivo* in a mouse xenograft

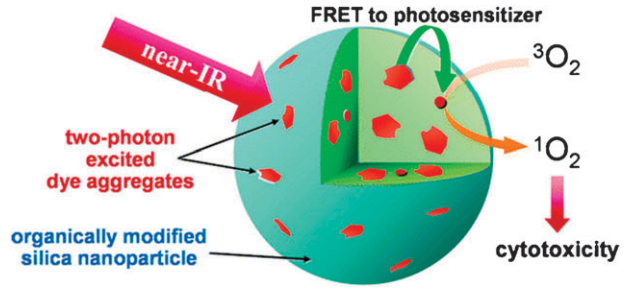

Fig. 15 Schematic showing an organically modified silica nanoparticle co-encapsulating a photosensitizing drug and two-photon absorbing fluorescent dye aggregates for two-photon photodynamic therapy.[106]

model. After intratumoral injection of the MB nanoparticles, fluorescent imaging of the mice revealed that the tumor region was clearly defined, and after laser treatment, the tumor became necrotic (Fig. 16).

Silica nanoparticles have been extensively studied as DNA carriers for gene therapy.[59,108–112] For example, Prasad and coworkers have developed a fluorescently labeled silica nanoparticle with a cationic surface coating.[111] Gel electrophoresis studies revealed that the particles efficiently bind DNA *via* electrostatic interactions and prevent enzymatic degradation of the encapsulated DNA. Confocal microscopy studies revealed that the nanoparticles were uptaken by cells *in vitro* with the released DNA migrating to the nucleus. Further *in vivo* studies showed that the particles were able to successfully transfect and modulate the activity of neural cells in a murine model.[112] The efficiency of transfection was equal to or exceeded that of a viral vector and no particle related toxicity was observed after 4 weeks.

Jiang and coworkers have reported a system of hollow chitosan-silica nanospheres fabricated in aqueous medium.[113] The anticancer drug doxorubicin was loaded within the interior of the nanosphere (8.9 wt%). Drug release was found to be pH sensitive, with minimal release occurring at pH = 7.4; however, at pH = 4, a value that can be found in a tumor site, the drug is rapidly released. Preliminary cytotoxicity assays demonstrated

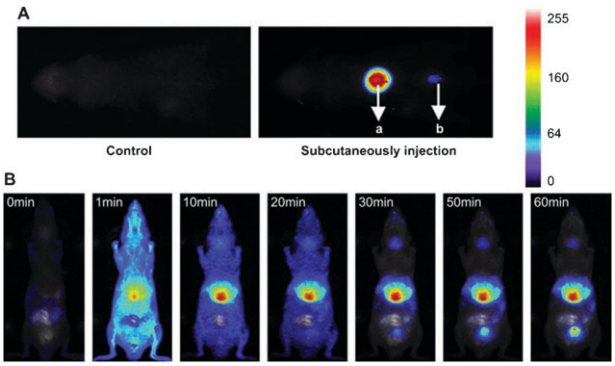

Fig. 16 (A) Images of control mice and the two subcutaneous injections of 100 μL MB-encapsulated PSiNPs with concentrations of 44 mg/mL (a) and 4.4 mg/mL (b). The acquisition was performed 2 min after injection. (B) Real-time *in vivo* abdomen imaging of mice intravenously injected with 200 μL of MB-encapsulated PSiNPs (44 mg/mL) at different time points, post injection. Reproduced with permission from ref. 107.

that the nanoparticles were more effective than doxorubicin, presumably by means of more efficient drug uptake. Corma and coworkers have developed liposomal doxorubicin nanoparticles with a poly(silsesquioxane) shell.[114] *In vitro* assays against human glioma cells demonstrated that the nanospheres were able to kill the cells, reaching mortality rates of 44%, compared to 90% for the free drug. Fluorescence microscopy images revealed that the nanospheres enter the cells and release doxorubicin.

4.2 Mesoporous silica nanoparticles for therapy

MSNs have been extensively evaluated as delivery vehicles for a variety of cargoes. Victor Lin and coworkers demonstrated the use of MCM-41 nanoparticles for the delivery of a membrane impermeable protein, cytochrome C.[66] After removing the surfactants from large-pore (5.4 nm) MSN particles, cytochrome C (maximum loading = 41.5 wt%) was loaded into the pores. The release of the protein was measured in PBS at two different pH values (7.4 and 5.2) over a 25 hour period. The total percentages of proteins that were released were 45 and 55% at pH values of 7.4 and 5.2, respectively. The difference in release was attributed to the extent of negative charge on the MSN surface, which favorably interacts with the positively charged protein. No significant release of the protein was detected within the first 4 hours at pH 7.4, which allows for the introduction of protein loaded particles into cell culture at physiological pH without losing a large amount of the entrapped protein due to burst release kinetics. The released cytochrome C was found to retain catalytic activity for the oxidation of 2,2′-azino-bis(3-ethylbenzthiazoline-6-sulfonate) (ABTS) by hydrogen peroxide. Efficient uptake of the particles was observed using HeLa cells, and confocal microscopy showed escape of the protein from endosomal entrapment. MSN systems were also used to deliver cysteine to cells.[115] The covalently attached cysteine does not release from the MSNs in the absence of a reducing agent; however, all cysteine was released within 1 h of the addition of a suitable reducing agent. *In vitro* assays against HeLa cells demonstrated that the conjugated nanoparticle was 444 times more effective at inhibiting cell growth than N-acetylcysteine, the standard molecule for cysteine therapy.

Victor Lin and coworkers have also developed several MSN-based delivery systems containing stimuli-responsive pore caps (such as CdS, Au, and superparamagnetic Fe_3O_4 nanoparticles) to allow for the controlled release of entrapped molecules.[116,117] As an example shown in Fig. 17, the gold nanoparticles were conjugated to the MSN materials with a photolabile linker.[118] The hybrid system will release the Au nanoparticle pore caps when exposed to UV. This system was used to deliver paclitaxel to human liver and fibroblast cells. After UV irradiation, significant decreases in cell viability were observed. Other drug molecules and neurotransmitters, such as vancomycin and adenosine triphosphate (ATP), have also been delivered using this strategy.[116,117]

A double drug delivery system was also developed based on capped MSN nanoparticles.[119] Boronic acid functionalized MSN nanoparticles were loaded with cyclic adenosine monophosphate (cAMP), an important cellular signaling molecule.

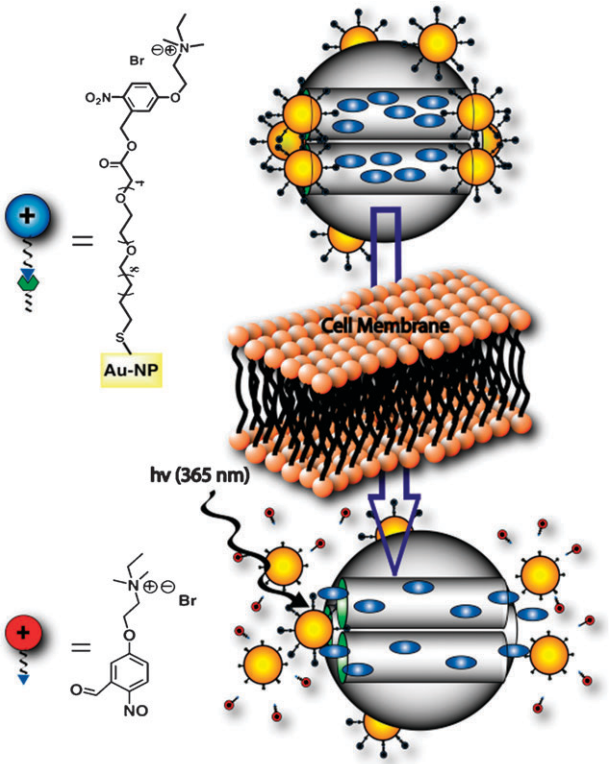

Fig. 17 Schematic representation of the Au nanoparticle-capped MSN-based drug delivery system. The controlled release mechanism of the system is based on UV irradiation.[118]

The pores of the material were then capped with fluorescein-labeled insulin. Release from the material was shown to be triggered by saccharides, as they form more stable conjugates with the boronic acids on the nanoparticles. In a 50 mM solution of glucose in PBS, 80% of the entrapped cAMP was released within 20 hours, with less than 10% released in the same time frame without glucose. Preliminary *in vitro* assays demonstrated that the materials showed low cytotoxicity and were able to deliver cAMP to pancreatic cells in a dose dependent manner.

Feng and coworkers demonstrated the use of a cross-linked polymer network as a "gatekeeper" for MSN (Fig. 18).[120] 2-nm thick poly(*N*-acryloxysuccinimide) was anchored to the MSN surface through reversible addition-fragmentation chain transfer (RAFT) polymerization and then cross-linked by adding cystamine. The ability to control the release of cargos was demonstrated by entrapping rhodamine B inside the MSN before cross-linking of the polymer. A light-activated nanoimpeller-controlled drug carrier based on MSNs was recently designed by taking advantage of the well known cis-trans isomerization in the azobenzene derivative (4-phenylazoaniline).[121] The anti-cancer drug camptothecin loaded into this system could be trigger released by irradiation at 413 nm. After incubating the cells with the drug-loaded MSN, cell death was only observed after irradiation. A related trigger release system based on MSN supported polyelectrolyte multilayers (PEM) was developed by Wang and coworkers for controlled delivery of doxorubicin *in vitro*.[122]

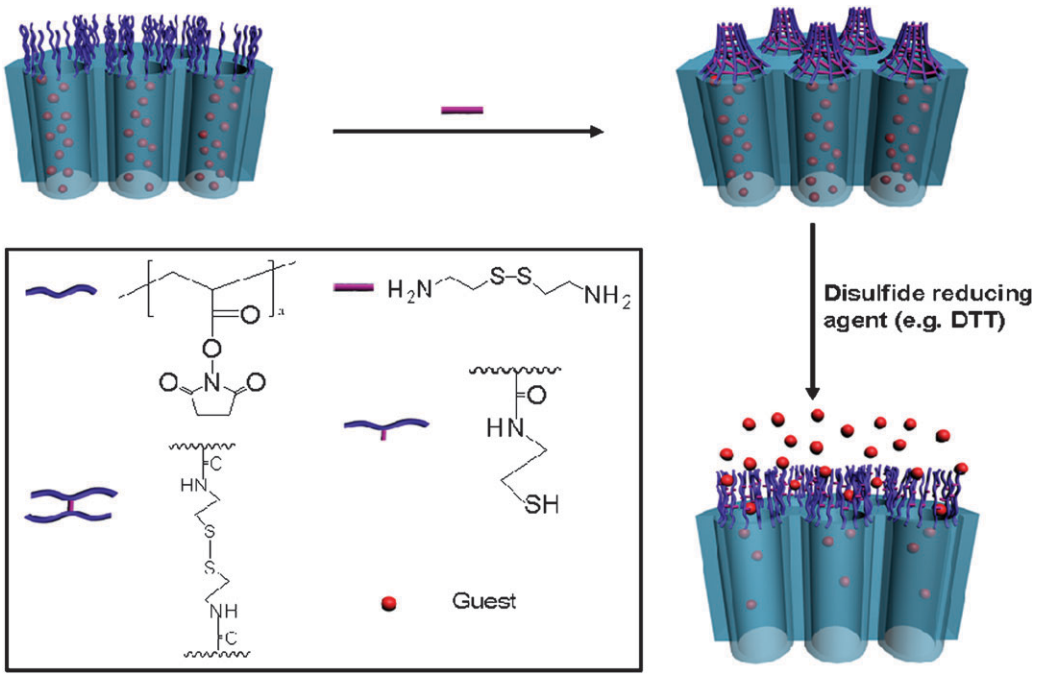

Fig. 18 Schematic illustration of redox responsive nanogated ensemble based on polymeric network-capped mesoporous silica.[120]

Brinker and coworkers have developed porous nanoparticle supported lipid bilayers (protocells) as delivery vehicles (Fig. 19).[123] Liposome fusion on mesoporous particles was utilized to simultaneously load and seal cargo within the porous core. With the use of a cationic lipid (DOTAP) on an anionic silica particle, an anionic fluorescent dye (calcein) was effectively loaded into the particles. The loaded protocell particles were taken up efficiently by Chinese hamster ovary (CHO) cells. Calcein was effectively released inside endosomal compartments due to a reduced pH. Brinker and coworkers have used the same approach to coat cationic MSNs.[124] A cationic mesoporous material was synthesized by incorporating 3-[2-(2-aminoethylamino)ethylamino]propyltriethoxysilane into the silica framework, and was then fused with anionic (DOPS) liposomes.

The protocell system was also adapted for gene delivery.[125] Cationic liposomes were fused with solid silica nanoparticles of 30, 50, 80, and 130 nm in diameter to form silica supported lipid bilayers. These particles were shown to bind to plasmid DNA in a size dependent manner, as measured by gel electrophoresis. It was observed that the transfection efficiency in the CHO cells decreased with particle size, with the 130 nm particles exhibiting no DNA transfection. These protocell constructs were found to protect the DNA from enzymatic degradation. Confocal microscopy studies revealed that the DNA needed to be released from the construct to induce transfection. For larger nanoparticles, the DNA appears to be trapped on the silica nanoparticles and does not leave the endosomal compartment, responsible for the lack of activity for the 130 nm nanoparticles.

Because of the ability to carry both imaging and therapeutic agents in a single particle platform, hybrid silica nanoparticles have also been explored for theranostic applications. Hyeon and coworkers synthesized particles containing a single iron

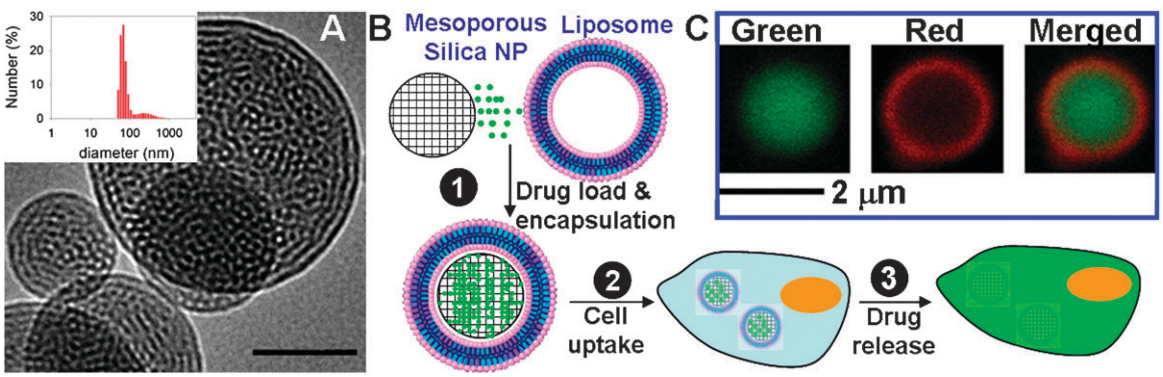

Fig. 19 (A) TEM image of MSN, scale bar = 50 nm. Inset shows the dynamic light scattering histogram for these particles. (B) Schematic representation of drug loading of MSN and encapsulation with a liposome to form a protocell, followed by cell uptake and drug release inside a cell. (C) Confocal images of the protocell: FITC-labeled MSN (green), Texas Red-labeled liposome (red), and the merged image showing the protocell. Reproduced with permission from ref. 123.

oxide nanoparticle coated with a mesoporous silica shell.[69] SPIO nanoparticles provide T_2-weighed MR contrast enhancement, while the mesoporous silica serves as a drug carrier. Fluorescent dyes were also covalently attached to the silica shell and the anticancer drug doxorubicin was loaded into the pores. Preliminary *in vitro* assays revealed that the carrier possessed minimal cytotoxicity to cancer cells, while the doxorubicin loaded nanoparticles showed a dose dependent cytotoxicity profile. *In vivo* assays on a murine xenograft model showed strong T_2 signal reduction at the tumor site up to 24 hours post injection, which was confirmed by *ex vivo* organ analysis by fluorescence microscopy (Fig. 20). A similar report by Zink and coworkers described the encapsulation of SPIO nanocrystals inside mesostructured silica spheres that were labeled with fluorescent dye molecules and coated with hydrophilic groups (trihydroxysilylpropyl methylphosphonate) to prevent aggregation.[67] Water-insoluble anticancer drugs (camptothecin and paclitaxel) were delivered into human cancer cells; surface conjugation with cancer-specific targeting agents increased the uptake into cancer cells relative to that in non-cancerous fibroblasts.

Chou, Chi, Hsiao, and coworkers have developed a multi-modal system for MR imaging and photodynamic therapy.[126] Silica-coated SPIO nanoparticles were functionalized with an iridium photosensitizer, and were evaluated *in vitro*. Confocal microscopy experiments revealed that the nanoparticles were efficiently uptaken by HeLa cells in a dose dependent fashion. The nanoparticles also provided adequate T_2-weighted contrast in a 1.5 T scanner. Cytotoxicity assays revealed that the as-synthesized nanoparticles were not cytotoxic in the absence of irradiation; however, they exhibited significant cell death upon irradiation.

4.3 Nanoscale metal–organic frameworks for therapy

Our group has recently demonstrated the use of NCPs as drug delivery vehicles.[81] NCPs based on a Pt-containing anticancer drug were synthesized using a rapid precipitation method, whereby a poor solvent was added to an aqueous solution of the precursors, DSCP and Tb^{3+}, to induce the formation of nanoparticles. In order to stabilize the particles against rapid dissolution, they were coated with a silica shell (Fig. 21). The half-life ($t_{1/2}$) for the release of DSCP, a cisplatin prodrug, from NCPs of the composition $Tb_2(DSCP)_3(H_2O)_{12}$ could be tuned from approximately 5.5 hours to 9 hours by increasing the shell thickness from approximately 2 nm to 7 nm. In comparison, the as-synthesized NCPs had a $t_{1/2}$ of only 1 hour.

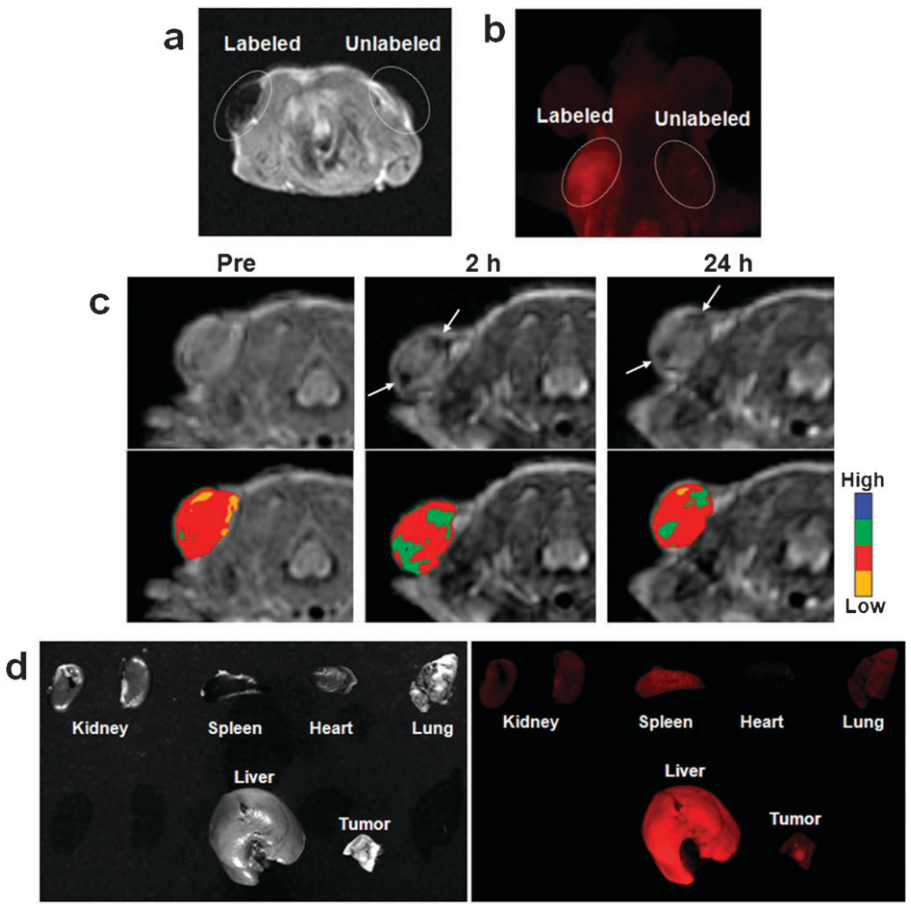

Fig. 20 *In vivo* T_2-weighted MR (a) and fluorescence (b) images of subcutaneously injected MCF-7 cells labeled with Fe_3O_4@MSN and control cells. (c) T_2-weighted MR (upper row) and color maps (lower row) of the tumor before and after the Fe_3O_4@MSN particles were intravenously injected into the tail vein of a nude mouse implanted with MCF-7 cells. A decrease in signal intensity was detected at the tumor site (arrows). (d) Photographic (left) and fluorescence (right) images of several organs and the tumor 24 hours after iv injection. Reproduced with permission from ref. 69.

In vitro cytotoxicity assays showed that the Pt-based NCP particles displayed anticancer efficacies superior to the cisplatin standards.

NMOF-based systems have also been developed for theranostic applications. Our group has demonstrated a post-synthesis modification scheme to introduce therapeutic and imaging moieties into the iron-carboxylate NMOF, MIL-101 (Fig. 22).[80] Highly porous MIL-101 nanoparticles with amine-functionality were synthesized using a solvothermal method with microwave heating. An optical imaging agent, 1,3,5,7-tetramethyl-4,4-difluoro-8-bromoethyl-4-bora-3a,4a-diaza-s-indacene (Br-Bodipy) was loaded into the framework by covalent attachment to the amine groups in the framework, achieving up to 11 wt% loading. This nanoparticle conjugate was coated with a layer of amorphous silica, which served to significantly retard the dissolution rate. Confocal microscopy experiments with the Bodipy-MIL-101 nanoparticles demonstrated fluorescent labeling of cells in a dose dependent manner. Control studies demonstrated that the Br-Bodipy conjugate by itself was not internalized by cells and no fluorescence was observed. A cisplatin prodrug, *c,c,t*-$Pt(NH_3)_2Cl_2(OEt)(O_2CCH_2CH_2COOH)$ was also covalently incorporated into the framework *via* an amide linkage between the amine groups in the framework and the carboxylate of the anti-cancer drug. These nanoparticles were encapsulated in amorphous silica and tested *in vitro* against HT-29 human colon adenocarcinoma cells. Treatment of the cells with the Pt-loaded MIL-101 showed appreciable cytotoxicity (IC_{50} = 29 μM), but not as much as cisplatin under the same conditions (IC_{50} = 20 μM). Targeting of the nanoparticles with a silyl-derived cyclic RGD peptide as a targeting moiety increased the cytotoxicity to a value comparable to cisplatin (IC_{50} = 21 μM).

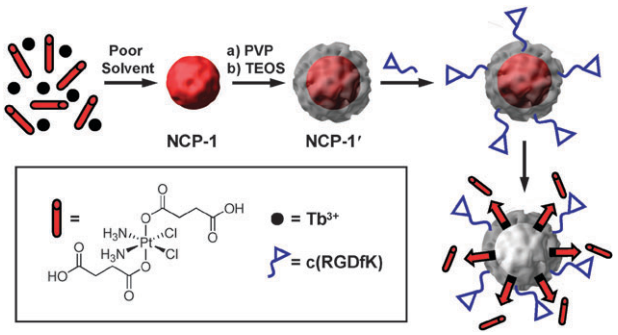

Fig. 21 Schematic showing controlled release of DSCP from the core–shell NCP nanostructure.[81]

Boyes and coworkers have developed a multimodal system for targeted imaging and treatment of cancer.[84] Gadolinium-based NMOF particles were synthesized as described previously[78] and were functionalized with PNIPAM-*co*-PNSOS-*co*-PFMA copolymers *via* vacant coordination sites on the Gd^{3+} metal centers. A chemotherapeutic, methotrexate (MTX), and a targeting peptide, glycine-arginine-glycine-aspartate-serine-NH_2 (GRGDS-NH_2) were conjugated to the copolymer. Preliminary *in vitro* assays were performed on canine FITZ-HSA cells. Confocal microscopy experiments

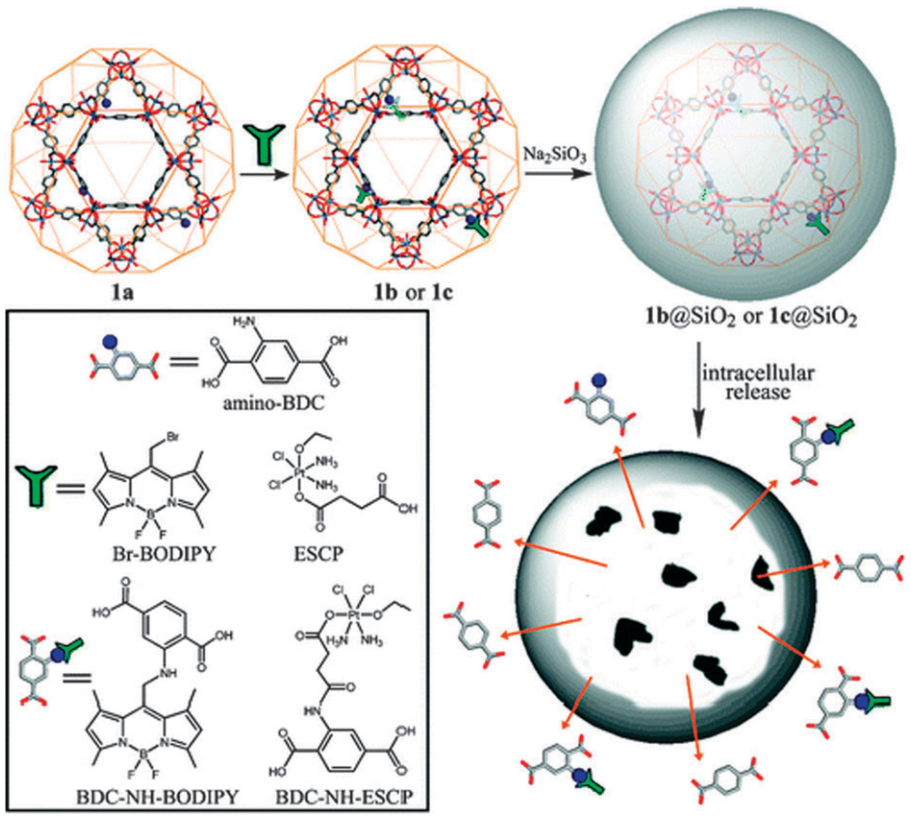

Fig. 22 Schematic of the post-synthetic modification of MIL-101-type nanoparticles to impart imaging or therapeutic functionality.[80]

demonstrated that the targeted nanoparticles had significant localization at the cell surface after 1 h of incubation, with internalization observed after 24 hours, while the unmodified nanoparticles had no significant fluorescence over the same time period. Cell growth inhibition studies demonstrated that the MTX-containing nanoparticles show a dose-dependent inhibition of growth similar to the free drug.

Horcajada and coworkers have developed a group of porous NMOF carriers for both drug delivery and imaging.[43] They synthesized five iron carboxylate NMOFs in aqueous phase (corresponding to the previously reported MIL-89, MIL-101_NH_2, MIL-88A, MIL-100, and MIL-53 bulk phases). These frameworks were rendered more biocompatible by coating with PEG, dextran, and chitosan. The MIL-88A particles showed low *in vitro* toxicity against murine macrophage cells (57 μg/mL). The *in vivo* toxicity of MIL-88A, MIL-100, MIL-88Bt was determined using the highest injectable amount (up to 220 mg/kg) in a rat model. Aside from a small increase of liver and spleen weights observed at the onset of the study (which returned to control levels after a short period of time), no signs of toxicity were observed for 3 months.

The particle systems were also evaluated as T_2-weighted MRI contrast agents. Mössbauer spectroscopy demonstrated that the NMOFs themselves, not any iron oxide or hydroxide decomposition products, acted as the contrast agents and had r_2 values up to 95 mM^{-1} s^{-1} for MIL-88A-PEG NMOFs.[43] *In vivo* studies using Wistar rats demonstrated that the particles showed negative contrast in the major RES organs (liver and spleen) 30 minutes post injection of MIL-88A nanoparticles. This contrast disappeared 3 months post injection.

These NMOFs were also evaluated as potential drug carriers. Four different anti-cancer or antiviral drugs (busulfan, azidothymidine triphosphate, cidofovir, and doxorubicin) were loaded into the NMOF pores *via* noncovalent interactions. This drug loading was highly efficient, with up to 90 wt% loading for azidothymidine triphosphate (AZT) into MIL-101_NH_2 particles. Release profile studies using MIL-100 nanoparticles loaded with cidofovir, doxorubicin, and AZT showed sustained release with no burst effects. The potential applicability of these NMOFs as drug delivery vehicles was evaluated *in vitro*. Experiments using human leukemia and myeloma cells showed that MIL-100 nanoparticles loaded with busulfan displayed comparable cytotoxicity to the free drug. Further *in vitro* tests using MIL-100 nanoparticles loaded with AZT showed significant anti-HIV activity only for those nanoparticles loaded with the active drug, with the nanocarrier showing no significant activity over the same concentration range.

5. Conclusions

Hybrid materials are emerging as powerful platforms for biomedical applications. The inclusion of organic and inorganic components within a single system allows these materials to be modified for a multitude of applications. Silica based materials, both solid and porous, are being developed as imaging, therapeutic, and theranostic materials. These materials can be customized with numerous functionalities tailored to specific physical properties and applications. An extensive amount of *in vitro* evidence demonstrates the advantages of these platforms over small molecule agents; their *in vivo* efficacy has also been recently demonstrated. Further work is necessary to demonstrate *in vivo* efficacy and improved pharmacokinetics before these materials advance into clinical application.

The development of NMOFs as biomaterials is still in its infancy, with only a few examples of these materials in the literature. NMOFs possess nearly infinite tunability for specific applications and are intrinsically biodegradable. Preliminary *in vitro* and *in vivo* assays show the potential biomedical use of these materials and continued development will render these materials as relevant platforms for potential applications in the clinic.

Acknowledgements

We would like to thank Dr Juan Vivero-Escoto for help with graphics. We acknowledge funding support from NIH and NSF.

References

1 M. Ferrari, *Nat. Rev. Cancer*, 2005, **5**, 161–171.
2 K. Cho, X. Wang, S. Nie, Z. Chen and D. M. Shin, *Clin. Cancer Res.*, 2008, **14**, 1310–1316.
3 M. E. Davis, Z. Chen and D. M. Shin, *Nat. Rev. Drug Discovery*, 2008, **7**, 771–782.
4 D. Peer, J. M. Karp, S. Hong, O. C. Farokhzad, R. Margalit and R. Langer, *Nat. Nanotechnol.*, 2007, **2**, 751–760.
5 S. Laurent, D. Forge, M. Port, A. Roch, L. Vander Elst and R. N. Muller, *Chem. Rev.*, 2008, **108**, 2064–2110.
6 F. Alexis, E. Pridgen, L. K. Molnar and O. C. Farokhzad, *Mol. Pharmaceutics*, 2008, **5**, 505–515.
7 S. D. Li and L. Huang, *Mol. Pharmaceutics*, 2008, **5**, 496–504.
8 V. P. Torchilin, *Nat. Rev. Drug Discovery*, 2005, **4**, 145–160.
9 A. M. Smith, H. Duan, A. M. Mohs and S. Nie, *Adv. Drug Delivery Rev.*, 2008, **60**, 1226–1240.
10 W. W. Yu, E. Chang, R. Drezek and V. L. Colvin, *Biochem. Biophys. Res. Commun.*, 2006, **348**, 781–786.
11 J. Weng and J. Ren, *Curr. Med. Chem.*, 2006, **13**, 897–909.
12 H. Zhang, D. Yee and C. Wang, *Nanomedicine*, 2008, **3**, 83–91.
13 V. Biju, T. Itoh, A. Anas, A. Sujith and M. Ishikawa, *Anal. Bioanal. Chem.*, 2008, **391**, 2469–2495.
14 M. S. Yavuz, Y. Cheng, J. Chen, C. M. Cobley, Q. Zhang, M. Rycenga, J. Xie, C. Kim, K. H. Song, A. G. Schwartz, L. V. Wang and Y. Xia, *Nat. Mater.*, 2009, **8**, 935–939.
15 M. Hu, J. Chen, Z. Y. Li, L. Au, G. V. Hartland, X. Li, M. Marquez and Y. Xia, *Chem. Soc. Rev.*, 2006, **35**, 1084–1094.
16 P. K. Jain, X. Huang, I. H. El-Sayed and E.-S. M. A., *Acc. Chem. Res.*, 2008, **41**, 1578–1586.
17 E. Boisselier and D. Astruc, *Chem. Soc. Rev.*, 2009, **38**, 1759–1782.
18 W. J. M. Mulder, G. J. Strijkers, G. A. F. van Tilborg, D. P. Cormode, Z. A. Fayad and K. Nicolay, *Acc. Chem. Res.*, 2009, **42**, 904–914.
19 K. N. J. Burger, R. W. H. M. Staffhorst, H. C. de Vijlder, M. J. Velinova, P. H. Bomans, P. M. Frederik and B. de Kruijff, *Nat. Med.*, 2002, **8**, 81–84.
20 V. P. Torchilin, *Adv. Drug Delivery Rev.*, 1997, **24**, 301–313.
21 D. B. Stanimirovic, M. Markovic, D. V. Micic, M. Spatz and B. B. Mrsulka, *Neurochem. Res.*, 1994, **19**, 1473–1478.
22 Y. C. Tseng, S. Mozumdar and L. Huang, *Adv. Drug Delivery Rev.*, 2009, **61**, 721–731.
23 S. Nayak and L. A. Lyon, *Angew. Chem., Int. Ed.*, 2005, **44**, 7686–7708.
24 M. Hidaka, T. Kanematsu, K. Ushio and J. Sunamoto, *J. Bioact. Compat. Polym.*, 2006, **21**, 591–602.
25 D. Gao, H. Xu, M. A. Philbert and R. Kopelman, *Angew. Chem., Int. Ed.*, 2007, **46**, 2224–2227.

26 K. McAllister, P. Sazani, M. Adam, M. J. Cho, M. Rubinstein, R. J. Samulski and J. M. DeSimone, *J. Am. Chem. Soc.*, 2002, **124**, 15198–15207.
27 H. Dai, Q. Chen, H. Qin, Y. Guan, D. Shen, Y. Hua, Y. Tang and J. Xu, *Macromolecules*, 2006, **39**, 6584–6589.
28 N. Sahiner, A. M. Alb, R. Graves, T. Mandal, G. L. McPherson, W. F. Reed and V. T. John, *Polymer*, 2007, **48**, 704–711.
29 D. Missirlis, R. Kawamurab, N. Tirelli and J. A. Hubbell, *Eur. J. Pharm. Sci.*, 2006, **29**, 120–129.
30 M. Hamidi, A. Azadi and P. Rafiei, *Adv. Drug Delivery Rev.*, 2008, **60**, 1638–1649.
31 F. Chiellini, C. Bartoli, D. Dinucci, A. M. Piras, R. Anderson and T. Croucher, *Int. J. Pharm.*, 2007, **343**, 90–97.
32 Y. Zeng and W. G. Pitt, *J. Biomater. Sci., Polym. Ed.*, 2005, **16**, 371–380.
33 R. Duncan, *Nat. Rev. Cancer*, 2006, **6**, 688–702.
34 C. C. Lee, J. A. MacKay, J. M. Frechet and F. C. Szoka, *Nat. Biotechnol.*, 2005, **23**, 1517–1526.
35 U. Gupta, H. B. Agashe, A. Asthana and N. K. Jain, *Nanomed.: Nanotechnol., Biol. Med.*, 2006, **2**, 66–73.
36 H. Yang, S. T. Lopina, L. P. DiPersio and S. P. Schmidt, *J. Mater. Sci.: Mater. Med.*, 2008, **19**, 1991–1997.
37 R. Kunii, H. Onishi and Y. Machida, *European Journal of Pharmacuetical Sciences*, 2007, **67**, 9–17.
38 A. Yang, L. Yang, W. Liu, S. Li, H. Xua and X. Yang, *Int. J. Pharm.*, 2007, **331**, 123–132.
39 J. Cheng, B. A. Teply, I. Sherifi, J. Sung, G. Luther, F. X. Gu, E. Levy-Nissenbaum, A. F. Radovic-Moreno, R. Langer and O. C. Farokhzad, *Biomaterials*, 2007, **28**, 869–876.
40 W. Lin, W. J. Rieter and K. M. L. Taylor, *Angew. Chem., Int. Ed.*, 2009, **48**, 650–658.
41 R. C. Huxford, J. Della Rocca and W. Lin, *Curr. Opin. Chem. Bio.*, 2010, in press.
42 J. An, S. J. Geib and N. L. Rosi, *J. Am. Chem. Soc.*, 2009, **131**, 8376–8377.
43 P. Horcajada, T. Chalati, C. Serre, B. Gillet, C. Sebrie, T. Baati, J. F. Eubank, D. Heurtaux, P. Clayette, C. Kreuz, J. S. Chang, Y. K. Hwang, V. Marsaud, P. N. Bories, L. Cynober, S. Gil, G. Ferey, P. Couvreur and R. Gref, *Nat. Mater.*, 2010, **9**, 172–178.
44 P. Horcajada, C. Serre, G. Maurin, N. A. Ramsahye, F. Balas, M. Vallet-Regi, M. Sebban, F. Taulelle and G. Ferey, *J. Am. Chem. Soc.*, 2008, **130**, 6774–6780.
45 P. Horcajada, C. Serre, M. Vallet-Regi, M. Sebban, F. Taulelle and G. Ferey, *Angew. Chem., Int. Ed.*, 2006, **45**, 5974–5978.
46 L. Wang, W. Zhao and W. Tan, *Nano Res.*, 2008, **1**, 99–115.
47 L. Wang, K. Wang, S. Santra, X. Zhao, L. R. Hilliard, J. E. Smith, Y. Wu and W. Tan, *Anal. Chem.*, 2006, **78**, 646–654.
48 Y. Jin, A. Li, S. G. Hazelton, S. Liang, C. L. John, P. D. Selid, D. T. Pierce and J. X. Zhao, *Coord. Chem. Rev.*, 2009, **253**, 2998–3014.
49 W. Stober, A. Fink and E. Bohn, *J. Colloid Interface Sci.*, 1968, **26**, 62–69.
50 X. D. Wang, Z. X. Shen, T. Sang, X. B. Cheng, M. F. Li, L. Y. Chen and Z. S. Wang, *J. Colloid Interface Sci.*, 2010, **341**, 23–29.
51 F. J. Arriagada and K. Osseo-Asare, *Colloids Surf.*, 1992, **69**, 105–115.
52 F. J. Arriagada and K. Osseo-Asare, *J. Colloid Interface Sci.*, 1999, **211**, 210–210.
53 W. J. Rieter, J. S. Kim, K. M. L. Taylor, H. An, T. Tarrant and W. Lin, *Angew. Chem., Int. Ed.*, 2007, **46**, 3680–3682.
54 Y. S. Chung, M. Y. Jeon and C. K. Kim, *Macromol. Res.*, 2009, **17**, 37–43.
55 R. P. Bagwe, C. Yang, L. R. Hilliard and W. Tan, *Langmuir*, 2004, **20**, 8336–8342.
56 D. Ma, J. Guan, F. Normandin, S. De'nomme'e, G. Enright, T. Veres and B. Simard, *Chem. Mater.*, 2006, **18**, 1920–1927.
57 J. L. Bridot, A. C. Faure, S. Laurent, C. Rivire, C. Billotey, B. Hiba, M. Janier, V. Josserand, J. L. Coll, L. Vander Elst, R. Muller, S. Roux, P. Perriat and O. Tillement, *J. Am. Chem. Soc.*, 2007, **129**, 5076–5084.
58 D. Gerion, J. Herberg, R. Bok, E. Gjersing, E. Ramon, R. Maxwell, J. Kurhanewicz, T. F. Budinger, J. W. Gray, M. A. Shuman and F. F. Chen, *J. Phys. Chem. C*, 2007, **111**, 12542–12551.
59 Slowing, II, J. L. Vivero-Escoto, C. W. Wu and V. S. Y. Lin, *Adv. Drug Delivery Rev.*, 2008, **60**, 1278–1288.
60 B. G. Trewyn, I. Slowing, S. Giri, H. T. Chen and V. S. Y. Lin, *Acc. Chem. Res.*, 2007, **40**, 846–853.
61 C. T. Kresge, M. E. Leonowicz, W. J. Roth, J. C. Vartuli and J. S. Beck, *Nature*, 1992, **359**, 710–712.
62 M. Grun, K. K. Unger, A. Matsumoto and K. Tsutsumi, *Microporous Mesoporous Mater.*, 1999, **27**, 207–216.
63 Q. Cai, Z. S. Luo, W. Q. Pang, Y. W. Fan, X. H. Chen and F. Z. Cui, *Chem. Mater.*, 2001, **13**, 258–263.
64 H. T. Chen, S. Huh, J. W. Wiench, M. Pruski and V. S. Y. Lin, *J. Am. Chem. Soc.*, 2005, **127**, 13305–13311.
65 I. Slowing, B. G. Trewyn and V. S. Y. Lin, *J. Am. Chem. Soc.*, 2006, **128**, 14792–14793.
66 I. Slowing, B. G. Trewyn and V. S. Y. Lin, *J. Am. Chem. Soc.*, 2007, **129**, 8845–8849.
67 M. Liong, J. Lu, M. Kovochich, T. Xia, S. G. Ruehm, A. E. Nel, F. Tamanoi and J. I. Zink, *ACS Nano*, 2008, **2**, 889–896.
68 Y. S. Lin, Y. Hung, J. K. Su, R. Lee, C. Chang, M. L. Lin and C. Y. Mou, *J. Phys. Chem. B*, 2004, **108**.
69 J. Kim, H. S. Kim, N. Lee, T. Kim, H. Kim, T. Yu, I. C. Song, W. K. Moon and T. Hyeon, *Angew. Chem., Int. Ed.*, 2008, **47**, 8438–8441.
70 K. M. L. Taylor, J. S. Kim, W. J. Rieter, H. An, W. Lin and W. Lin, *J. Am. Chem. Soc.*, 2008, **130**, 2154–2155.
71 S. Huh, J. W. Wiench, B. G. Trewyn, S. Song and V. S. Y. Lin, *Chem. Commun.*, 2003, 2364–2365.
72 S. Huh, J. W. Wiench, J. C. Yoo, M. Pruski and V. S. Y. Lin, *Chem. Mater.*, 2003, **15**, 4247–4256.
73 O. R. Evans and W. Lin, *Acc. Chem. Res.*, 2002, **35**, 511–522.
74 L. Ma, C. Abney and W. Lin, *Chem. Soc. Rev.*, 2009, **38**, 1248–1256.
75 J. L. C. Rowsell and O. M. Yaghi, *Angew. Chem., Int. Ed.*, 2005, **44**, 4670.
76 D. Mircea and J. R. Long, *Angew. Chem., Int. Ed.*, 2008, **47**, 6766.
77 B. Chen, L. Wang, Y. Xio, F. R. Fronczek, M. Xue, Y. Cui and G. Qian, *Angew. Chem., Int. Ed.*, 2009, **48**, 500–503.
78 W. J. Rieter, K. M. L. Taylor, H. An, W. Lin and W. Lin, *J. Am. Chem. Soc.*, 2006, **128**, 9024–9025.
79 K. M. L. Taylor, A. Jin and W. Lin, *Angew. Chem., Int. Ed.*, 2008, **47**, 7722–7725.
80 K. M. L. Taylor-Pashow, J. Della Rocca, Z. Xie, S. Tran and W. Lin, *J. Am. Chem. Soc.*, 2009, **131**, 14261–14263.
81 W. J. Rieter, K. M. Pott, K. M. L. Taylor and W. Lin, *J. Am. Chem. Soc.*, 2008, **130**, 11584–11585.
82 W. J. Rieter, K. M. L. Taylor and W. Lin, *J. Am. Chem. Soc.*, 2007, **129**, 9852–9853.
83 K. M. L. Taylor, W. J. Rieter and W. Lin, *J. Am. Chem. Soc.*, 2008, **130**, 14358–14359.
84 M. D. Rowe, D. H. Thamm, S. L. Kraft and S. G. Boyes, *Biomacromolecules*, 2009, **10**, 983–993.
85 S. Santra, H. Yang, D. Dutta, J. T. Stanley, P. H. Holloway, W. Tan, B. M. Moudgil and R. A. Mericle, *Chem. Commun.*, 2004, 2810–2811.
86 H. Ow, D. R. Larson, M. Srivastava, B. A. Baird, W. W. Webb and U. Wiesner, *Nano Lett.*, 2005, **5**, 113–117.
87 J. Choi, A. A. Burns, R. M. Williams, Z. Zhou, A. Fleskin-Nikitin, W. R. Zipfel, U. Wiesner and A. Y. Nikitin, *J. Biomed. Opt.*, 2007, **12**, 064007–064001-064011.
88 J. E. Fuller, G. T. Zugates, L. S. Ferreira, H. S. Ow, N. N. Nguyen, U. B. Wiesner and R. S. Langer, *Biomaterials*, 2008, **29**, 1526–1532.
89 M. Nakamura, M. Shono and K. Ishimura, *Anal. Chem.*, 2007, **79**, 6507–6514.
90 A. A. Burns, J. Vider, H. Ow, E. Herz, O. Penate-Medina, M. Baumgart, S. M. Larson, U. Wiesner and M. Bradbury, *Nano Lett.*, 2009, **9**, 442–448.
91 R. Kumar, I. Roy, T. Y. Ohulchanskyy, L. N. Goswami, A. C. Bonoiu, E. J. Bergey, K. M. Tramposch, A. Maitra and P. N. Prasad, *ACS Nano*, 2008, **2**, 449–456.
92 J. Qian, X. Li, M. Wei, X. Gao, Z. Xu and S. He, *Opt. Express*, 2008, **16**, 19568–19578.
93 L. Wang and W. Tan, *Nano Lett.*, 2006, **6**, 84–88.

94 S. Santra, P. Zhang, K. Wang, R. Tapec and W. Tan, *Anal. Chem.*, 2001, **73**, 4988–4993.
95 X. He, H. Nie, K. Wang, W. Tan, X. Wu and P. Zhang, *Anal. Chem.*, 2008, **80**, 9597–9603.
96 J. S. Kim, H. An, W. J. Rieter, D. Esserman, K. M. L. Taylor-Pashow, R. B. Sartor, W. Lin, W. Lin and T. K. Tarrant, *Clin. Exp. Rheum.*, 2009, **27**, 580–586.
97 J. S. Kim, W. J. Rieter, K. M. L. Taylor, H. An, W. Lin and W. Lin, *J. Am. Chem. Soc.*, 2007, **129**, 8962–8963.
98 C. Louis, R. Bazzi, C. A. Marquette, J. L. Bridot, S. Roux, G. Ledoux, B. Mercier, L. Blum, P. Perriat and O. Tillement, *Chem. Mater.*, 2005, **17**, 1673–1682.
99 P. Voisin, E. J. Ribot, S. Miraux, A. K. Bouzier-Sore, J. F. Lahitte, V. Bouchaud, S. Mornet, E. Thiaudie're, J. M. Franconi, L. Raison, C. Labruge're and M. H. Delville, *Bioconjugate Chem.*, 2007, **18**, 1053–1063.
100 R. Koole, M. M. Van Schooneveld, J. Hilhorst, K. Castermans, D. P. Cormode, G. J. Strijkers, C. de Mello Doneg, D. Vanmaekelbergh, A. W. Griffioen, K. Nicolay, Z. A. Fayad, A. N. Meijerink and W. J. M. Mulder, *Bioconjugate Chem.*, 2008, **19**, 2471–2479.
101 M. M. van Schooneveld, E. Vucic, R. Koole, Y. Zhou, J. Stocks, D. P. Cormode, C. Y. Tang, R. E. Gordon, K. Nicolay, A. N. Meijerink, Z. A. Fayad and W. J. M. Mulder, *Nano Lett.*, 2008, **8**, 2517–2525.
102 J. K. Hsiao, C. P. Tsai, T. H. Chung, Y. Hung, M. Yao, H. M. Liu, C. Y. Mou, C. S. Yang, Y. C. Chen and D. M. Huang, *Small*, 2008, **4**, 1445–1452.
103 J. M. Rosenholm, A. Meinander, E. Peuhu, R. Niemi, J. E. Eriksson, C. Sahlgren and M. Linden, *ACS Nano*, 2009, **3**, 197–206.
104 J. M. Rosenholm, E. Peuhu, J. E. Eriksson, C. Sahlgren and M. Linden, *Nano Lett.*, 2009, **9**, 3308–3311.
105 K. E. deKrafft, Z. Xie, G. Cao, S. Tran, L. Ma, O. Z. Zhou and W. Lin, *Angew. Chem., Int. Ed.*, 2009, **48**, 9901–9904.
106 S. Kim, T. Y. Ohulchanskyy, H. E. Pudavar, R. K. Pandey and P. N. Prasad, *J. Am. Chem. Soc.*, 2007, **129**, 2669–2675.
107 X. X. He, X. Wu, K. M. Wang, B. H. Shi and L. Hai, *Biomaterials*, 2009, **30**, 5601–5609.
108 V. Sokolova and M. Epple, *Angew. Chem., Int. Ed.*, 2008, **47**, 1382–1395.
109 M. A. Mintzer and E. E. Simanek, *Chem. Rev.*, 2009, **109**, 259–302.
110 C. Hom, J. Lu and F. Tamanoi, *J. Mater. Chem.*, 2009, **19**, 6308–6316.
111 I. Roy, T. Y. Ohulchanskyy, D. J. Bharali, H. E. Pudavar, R. A. Mistretta, N. Kaur and P. N. Prasad, *Proc. Natl. Acad. Sci. U. S. A.*, 2005, **102**, 11539–11544.
112 D. J. Bharali, I. Klejbor, E. K. Stachowiak, D. Dutta, I. Roy, N. Kaur, E. J. Bergey, P. N. Prasad and M. K. Stachowiak, *Proc. Natl. Acad. Sci. U. S. A.*, 2005, **102**, 11539–11544.
113 E. Yun, Y. Ding, C. Chen, R. Li, Y. Hu and X. Jiang, *Chem. Commun.*, 2009, 2718–2720.
114 A. Corma, U. Diaz, M. Arrica, E. Fernandez and I. Ortega, *Angew. Chem., Int. Ed.*, 2009, **48**, 6247–6250.
115 R. Mortera, J. L. Vivero-Escoto, I. Slowing, E. Garrone, B. Onida and V. S. Y. Lin, *Chem. Commun.*, 2009, 3219–3221.
116 C. Y. Lai, B. G. Trewyn, D. M. Jeftinija, K. Jeftinija, S. Xu, S. Jeftinija and V. S. Y. Lin, *J. Am. Chem. Soc.*, 2003, **125**, 4451–4459.
117 S. Giri, B. G. Trewyn, M. P. Stellmaker and V. S. Y. Lin, *Angew. Chem., Int. Ed.*, 2005, **44**, 5038–5044.
118 J. L. Vivero-Escoto, I. I. Slowing, C. W. Wu and V. S. Y. Lin, *J. Am. Chem. Soc.*, 2009, **131**, 3462–3463.
119 Y. Zhao, B. G. Trewyn, I. Slowing and V. S. Y. Lin, *J. Am. Chem. Soc.*, 2009, **131**, 8398–8400.
120 R. Liu, X. Zhao, T. Wu and P. Feng, *J. Am. Chem. Soc.*, 2008, **130**, 14418–14419.
121 J. Lu, E. Choi, F. Tamanoi and J. I. Zink, *Small*, 2008, **4**, 421–426.
122 C. L. Zhu, X. Y. Song, W. H. Zhou, H. H. Yang, Y. H. Wen and X. R. Wang, *J. Mater. Chem.*, 2009, **19**, 7765–7770.
123 J. Liu, A. Stace-Naughton, X. Jiang and C. J. Brinker, *J. Am. Chem. Soc.*, 2009, **131**, 1354–1355.
124 J. Liu, X. Jiang, C. Ashley and C. J. Brinker, *J. Am. Chem. Soc.*, 2009, **131**, 7567–7570.
125 J. Liu, A. Stace-Naughton and C. J. Brinker, *Chem. Commun.*, 2009, 5100–5102.
126 C. U. Lai, Y. H. Wang, C. H. Lai, M. J. Yang, C. Y. Chen, P. T. Chou, C. S. Chan, Y. Chi, Y. C. Chen and J. K. Hsiao, *Small*, 2008, **4**, 218–224.